A Non Linear Frequency Domain-Spectral Difference Scheme for Unsteady Periodic Flows

Jean-Sébastien Cagnone
Supervised by Siva K. Nadarajah

Masters of Engineering

Mechanical Engineering Department

McGill University

Montreal,Quebec

2008-10-20

A thesis submitted to McGill University in partial fulfilment of the requirements for the degree of Masters of Engineering

Library and Archives
Canada

Published Heritage
Branch

395 Wellington Street
Ottawa ON K1A 0N4
Canada

Bibliothèque et
Archives Canada

Direction du
Patrimoine de l'édition

395, rue Wellington
Ottawa ON K1A 0N4
Canada

Your file Votre référence
ISBN: 978-0-494-66918-1
Our file Notre référence
ISBN: 978-0-494-66918-1

NOTICE:

The author has granted a non-exclusive license allowing Library and Archives Canada to reproduce, publish, archive, preserve, conserve, communicate to the public by telecommunication or on the Internet, loan, distribute and sell theses worldwide, for commercial or non-commercial purposes, in microform, paper, electronic and/or any other formats.

The author retains copyright ownership and moral rights in this thesis. Neither the thesis nor substantial extracts from it may be printed or otherwise reproduced without the author's permission.

AVIS:

L'auteur a accordé une licence non exclusive permettant à la Bibliothèque et Archives Canada de reproduire, publier, archiver, sauvegarder, conserver, transmettre au public par télécommunication ou par l'Internet, prêter, distribuer et vendre des thèses partout dans le monde, à des fins commerciales ou autres, sur support microforme, papier, électronique et/ou autres formats.

L'auteur conserve la propriété du droit d'auteur et des droits moraux qui protège cette thèse. Ni la thèse ni des extraits substantiels de celle-ci ne doivent être imprimés ou autrement reproduits sans son autorisation.

In compliance with the Canadian Privacy Act some supporting forms may have been removed from this thesis.

While these forms may be included in the document page count, their removal does not represent any loss of content from the thesis.

Conformément à la loi canadienne sur la protection de la vie privée, quelques formulaires secondaires ont été enlevés de cette thèse.

Bien que ces formulaires aient inclus dans la pagination, il n'y aura aucun contenu manquant.

Canada

ACKNOWLEDGEMENTS

First and foremost, I would like to thank my research supervisor, Professor Siva K. Nadarajah, whose invaluable knowledge, experience and dedication supported me during this project. Through his guidance, he taught me to think for myself and to pursue my own ideas, which is without doubt, the most valuable gift a teacher can offer.

I would also like to recognize and express my gratitude to two special mentors. The first is my former aerodynamics teacher, Dr. Eric Laurendeau, who conveyed with boundless enthusiasm his expertise in CFD, and encouraged me to undertake graduate studies. The second is my undergraduate research supervisor, Dr. Mourad Heniche, whose attentive direction laid the grounds for a successful graduate experience.

This work has benefited from the generous support of the *Fonds de recherche sur la nature et les technologies.*

ABSTRACT

This research presents a new, more efficient computational scheme for complex periodic flows, and brings forward two novel ideas. The first consists in the use of a Fourier space time representation in conjunction with a high-order spatial discretization. The second is based on the efficient treatment of the resulting set of equations using a fast, implicit solver. This thesis describes the formulation and implementation of the proposed framework. Firstly, a high-order spectral difference scheme for the Euler equations is introduced. Secondly, the non-linear frequency domain method resolving the unsteady behavior of the flow is discussed. Thirdly, a mathematical and experimental validation of the proposed algorithm is carried out. Numerical experiments performed in this thesis suggest that the methodology could be an attractive new avenue for large scale time-dependent problems, alleviating the computational cost traditionally associated with such simulations.

ABRÉGÉ

Cette recherche présente un nouveau schéma numérique destiné aux écoulements périodiques complexes et met de l'avant deux nouvelles idées. La première consiste en l'utilisation d'une représentation temporelle en série de Fourier, liée à une discretisation spatiale d'ordre élevé. La seconde repose sur le traitement efficace des équations obtenues, grâce à l'utilisation d'une méthode itérative implicite. En premier lieu, cette thèse introduit le schéma d'ordre élevé intitulé "différence spectrale". En second lieu, nous présentons la méthode non-linéaire du domaine des fréquences utilisée pour calculer les effets non-stationnaires. En dernier lieu, on réalise une validation mathématique et expérimentale du schéma. Les simulations effectuées suggèrent que cette méthodologie est une alternative attrayante, permettant de réduire les coûts de calcul traditionnellement associés aux problèmes instationnaires complexes.

TABLE OF CONTENTS

LIST OF TABLES

LIST OF FIGURES

CHAPTER 1
Introduction

High-fidelity simulation of periodic flows is a challenging and computationally intensive task. Typically, one should ensure that the spatial features of the solution are all captured with adequate resolution. Similarly, all the relevant time-scales must also be present to accurately reflect the unsteady behavior of the physical system. Thus, for complex systems, these requirements will dictate the use of very fine spatial and temporal discretizations, leading to prohibitive computational costs that are unacceptable for practical applications.

A case of particular interest to aeronautical engineers is the simulation of helicopter rotors. Indeed, when sustaining forward flight, the rotor of an helicopter experiences complex flow situations. Due to the additional rotation-induced velocity, a shock wave develops on the advancing side of the rotor. On the retreating side, the blade's velocity relative to the air decreases and as the blade approaches the stall angle, a region of separated flow is generated. Furthermore, each blade of the rotor influences the next through the so-called blade-vortex interaction. Due to the pressure difference between the lower and upper side of the rotor, a vortex roll-up is created at the tip of each blade. The vortex shed by a blade travels downstream, eventually meeting the next incoming blade and changing its angle of incidence. Consequently, the global flow pattern is largely influenced by those interconnected flow phenomena, making reliable rotorcraft simulation notoriously challenging. Other equally difficult cases exist, and a non-exhaustive list includes vortical flows over multi-element airfoils, leading edge vortex shedding, flutter/buffet prediction and turbomachinery analysis. Although these cases have already been successfully studied, they represent the state-of-the-art in aerospace computational fluid dynamics (CFD) and would benefit from more efficient solution techniques.

In an effort to efficiently tackle complex flow simulations, the CFD and numerical analysis communities have been extensively exploring so-called *higher-order* methods. The rational behind high-order numerical schemes is that maximizing the accuracy of an algorithm is generally more cost-effective than employing the "brute force" solution of increasing the mesh density. In this work, this concept is employed in both space and time to create an accurate and efficient scheme for the simulation of periodic flows. The end goal of the research is the formulation of a novel approach where high-order schemes are employed to alleviate the simulation costs associated with the aforementioned applications, and allow the computation of previously intractable periodic problems. This chapter introducing numerical tools employed in this thesis is divided in three parts. Section (1.1) presents background material on high-order spatial discretizations for hyperbolic equations and discusses some of the established methodologies. Section (1.2) introduces spectrally accurate time representation methods for periodic flows, while section (1.3) enumerates the objectives of the present research.

1.1 High-Order Spatial Discretization

Second-order accurate finite-volume solvers have reached a level of maturity where large scale viscous computations can be realized within a few hours. However, for vortex dominated cases, second-order formulations are overly diffusive and fail to crisply capture the evolution of vortrical structures unless grid adaptation is used in the vicinity of the vortex. Trying to circumvent this limitation, many high-order alternatives have been proposed and shown to be significantly more effective.

To introduce these types of discretization along with the potential benefits, let us consider a generic high-order numerical method. This method is said to be of order k if the error in the approximated functional decays at the k^{th} power of the grid spacing h,

$$e \propto h^k.$$

Thus, when the grid density is doubled, the error of a fourth order solution decreases by a factor of 16, compared to a decrease of 4 for a second-order one. On the other hand, high-order solutions are also more expensive to compute and a fair comparison between low- and high-order methods can only be done by evaluating the error level with respect to the number of degrees-of-freedom (DOF) in the solution. For a scheme of fixed order, decreasing the mesh size, or *h-refinement*, results in a constant rate of convergence, qualified as *algebraic*. For a fixed grid, increasing the scheme's order, or *p-refinement*, results in an accelerating convergence rate, qualified as *exponential* or *spectral*. A generic convergence plot comparing algebraic and exponential convergence rates is presented in Fig. (1–1). From this simple argument, it follows that using high-order schemes is more effective than employing finer meshes. Indeed, for low error tolerances, high-order methods will require fewer degrees of freedom and therefore will be more efficient.

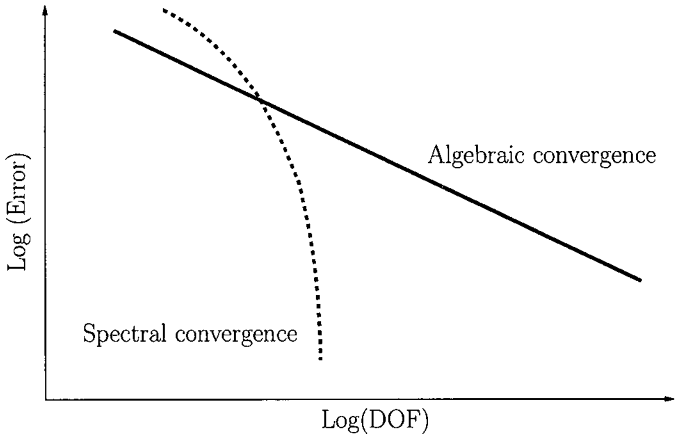

Figure 1–1: Illustration of algebraic and exponential convergence

The early attempts at creating high-order methods for compressible flows were deeply rooted in the pioneering work of Godunov [1]. His first-order numerical scheme assumed piecewise-constant flow variables that were discontinuous from cell to cell. Doing so, Godunov's method reduced the complex evolution of the gas-dynamics equations to Riemann initial value problems, where the interaction between two constant states needed to be considered. Godunov suggested to solve this simpler problem exactly, but its solution can also be approximated in some way. Later, Van Leer [2, 3] extended the scheme to second-order accuracy by introducing the MUSCL reconstruction technique. Using neighboring cells, his scheme estimated the solution's slope to correct the left and right state of each Riemann problem, allowing a piecewise-linear data representation. This extrapolation procedure can be used to achieve higher-order accuracy, as demonstrated by Colella and Woodward [4] who presented the third-order PPM formulation. Since then, numerous high-order schemes have been constructed by building upon the foundations laid by Godunov and Van Leer. In fact, literature on high-order methods is quite abundant and a thorough presentation of all numerical schemes falls well beyond the scope of this introduction, and only the most popular ones will be presented. A more complete description of established high-order schemes is given in the review papers of Ekaterinaris [5] and Wang [6] for structured and unstructured grids respectively.

In the late 1980's, Harten and Osher [7, 8] introduced an arbitrarily high-order extrapolation method, giving rise to the essentially non-oscillatory (ENO) scheme for hyperbolic equations. Similarly to Van Leer's MUSCL extrapolation, the ENO schemes employ a polynomial reconstruction using the information available in the neighborhood of a cell. However, if a sufficiently large set of neighbors is included in the stencil, the reconstruction is no longer unique and multiple polynomials with the desired order of accuracy may be computed. Harten and Osher's idea was to select the least oscillatory reconstruction available, thereby promoting stability near discontinuities. As a consequence of this choice, the ENO schemes present excellent accuracy and are oscillation-free in the limit of an infinitely fine computational mesh. Subsequently, extensions of the scheme to multidimensional and unstructured grids were considered by many researchers [9, 10, 11, 12, 13]. Although quite successful, the ENO schemes are hardly optimal since they select only one k^{th}−order accurate reconstruction based on the $2k-1$ points made available. To remedy this situation, Jiang and Shu [14] and Liu et al. [15] proposed the weighed essentially non-oscillatory (WENO) scheme designed to maximize the accuracy of ENO methods. In this scheme, the final extrapolated flow variable is given by a convex combination of all reconstruction stencils. The optimal combination is computed through weighting factors, themselves based on some smoothness norm. Near a discontinuity all weights but one go to zero, and the scheme chooses the least oscillatory stencil, recovering the ENO formulation. In smooth regions however, a weighted average of the possible stencils is used such that $2k-1^{\text{th}}$ order accuracy is achieved. In addition to accuracy benefits, the WENO method also presents smoother numerical fluxes and better convergence to steady-state than their ENO counterparts. The extension to unstructured grid was considered by Friedrich [16] and Hu and Shu [17]. A review of ENO and WENO schemes is presented in [18].

In parallel to ENO and WENO methods, another class of vastly popular high-order schemes was developed by applying the concept of numerical flux to the finite-element method (FEM). The idea of the so-called Discontinuous Galerkin (DG) method was first presented by Reed and Hill [19] to solve the neutron transport equation. In a series of papers, Cockburn and Shu [20, 21, 22, 23] extended the framework to compressible flows and Bassi and Rebay [24, 25] demonstrated the

DG method by obtaining formal high-order accuracy for Euler and Navier-Sokes equations. The revolutionary concept behind the DG scheme is the adoption of a flow representation that is discontinuous from one element to another, marking a major paradigm shift from the continuous Galerkin FEM. Inside the elements, a polynomial solution is formed by considering the product of discrete nodal values and nodal basis functions. These discrete values are updated by solving a variational statement arising from the weak form of the conservation law. The governing equation is multiplied by a test-function and integrated over the cell. Applying integration by parts leads to a volume integral and a surface flux integral. The volume and surface terms are evaluated through numerical quadrature as in the continuous Galerkin FEM, but the flux integration is calculated in a finite-volume (FV) fashion. At each face quadrature point, the left and right state is evaluated using the solution polynomial. There, a Riemann problem is solved to obtain the discrete numerical flux vector utilized in the quadrature. Employing this approach, adapted from the Godunov methods, is an elegant way of accounting for the wave-like structure of hyperbolic equations and stabilizes the finite-element approach that is otherwise unstable for convection-dominated flows. In recent literature, there has been a pronounced interest in the DG method due its particularly compact data representation. Indeed, unlike ENO and WENO methods, the high-order accuracy is achieved by including additional solution points at the element level. Accordingly, finite-difference reconstructions spanning multiple cells are traded for elemental basis functions, giving to the DG scheme the geometrical flexibility that finite element methods are known for. Moreover, the limited intercell coupling allows to vary the polynomial resolution from element to element, facilitating the implementation of hp-adaptive solvers. Finally, the compactness of the DG method is also advantageous to multiprocessor computing where it usually displays near-ideal parallelization efficiency. For a complete discussion of the history and development of the DG method refer to [26, 27] and the references therein.

Recently, other attractive alternatives to ENO/WENO and DG schemes have been proposed. Wang, Liu and their collaborators [28, 29, 30, 31, 32, 33] proposed the spectral volume (SV) method for hyperbolic conservation laws. This scheme is conceptually similar to the DG method as it also employs element-wise discontinuous polynomial solutions but differs in how its degrees of freedom are updated. Each spectral volume is subdivided in control volumes (CV) where the flow solution is piecewise-constant. Shape functions defining a high-degree polynomial are employed to interpolate the solution within the spectral volume. At the boundary of two CVs, the polynomial is smooth and the analytical flux vector is used to compute the local flux value. At the boundary between to adjacent spectral volumes, the data is usually discontinuous and a Riemann problem is solved to compute the flux. Once the discrete fluxes are obtained, high-order quadratures are used to integrate the fluxes and update the solution in a fashion similar to FV methods. The SV formulation is simpler and more intuitive than the DG scheme as no test function is involved. However, the extension to three-dimensional problems requires a large number of integration nodes and the method looses some of its efficiency. To eliminate this drawback, quadrature-free implementations have been explored [34].

Even simpler formulations may be derived by employing high-order difference schemes based on staggered-polynomials. This type of discretization was pioneered by Kopriva and Kolias [35, 36] as the staggered-grid multidomain method for structured meshes. In a later effort, Liu et al. [37] applied similar concepts and developed the spectral difference (SD) scheme for unstructured tetrahedral grids in an attempt to create a more efficient spectral volume scheme. Like the SV and DG methods, the solution is element-wise discontinuous but the equations are kept in differential form. Consequently, the formulation is free of test functions and quadrature rules, making it highly economical. Each cell is assigned a number of solution points and corresponding basis functions to create a high-degree polynomial. This polynomial is then utilized to extrapolate the solution to a second set of nodes holding the fluxes. Inside the cell, the analytical flux vector is evaluated, whereas a Riemann solver is employed where the solution is discontinuous. The fundamental difference with the SV method is that instead of integrating the fluxes, the SD scheme creates a second polynomial from discrete flux values. In turn, this polynomial is differentiated to compute the flux divergence needed for the residual evaluation. The extension of the SD scheme to the Euler and Navier-Stokes equations was established by Wang et al. [38] and May et al. [39]. Similarities between the SD scheme and DG and SV methods have been drawn by Huynh [40] and Van den Abeele et al. [41] respectively. Van den Abeele et al. [42] also presented a thorough analysis of the method and propose alternative nodal placements, leading to a broad class of possible SD schemes.

The high-order scheme for periodic flow presented in this thesis is based on the SD discretization method. This choice was motivated by the high-order that the scheme can achieve, and the availability of structured and unstructured formulations. By employing the differential form of the equations, the SD is both simpler and more efficient than the equivalent DG or SV schemes. Moreover, its compact data representation made it an attractive choice, providing additional flexibility over WENO discretizations of equivalent order. Finally, since all operations are performed at the element level, the developed NLFD-SD framework is largely independent of the type of SD implemented, and is applicable to all formulations as described by Van den Abeele et al. [42]; including the original staggered-grid multidomain method of Kopriva et al. [35, 36] and the unstructured SD of Liu et al. [37].

1.2 Spectral Temporal Representation

Most CFD algorithms are designed for very general problem statements. Typically, one distinguishes steady-state problems from time dependent ones, and chooses the solution algorithm on that basis. For steady cases, the fastest way to reach a converged state is sought and first-order implicit schemes are generally favored. For unsteady problems with large timescales, higher-order implicit schemes based on the backward difference formula or implicit Runge-Kutta methods allow large time-steps while maintaining good temporal accuracy. Finally, for unsteady problems where a fine sampling of the temporal spectrum is needed, explicit multistep integration schemes are the most efficient alternative. In the context of steady periodic flows however, the previously mentioned alternatives are far from optimal. Employing a time-accurate method requires an initial guess and the equations are integrated forward in time until the transient errors are sufficiently decayed. As a result, most of the effort is thus spent in achieving a periodic state, rather than sampling the true evolution of a flow period.

In 1993, Hall and Clark [43] approached periodic flow problems from a different perspective, suggesting a radical departure from time accurate methods. In their harmonic balance technique, the unsteady disturbances are assumed to be small and the flow variables are linearized about their mean value. Invoking the periodicity of the solution, the unsteady components of the solution are expanded in a Fourier series and solved for using a predetermined number of harmonics. The cost of an unsteady computation then becomes proportional to the cost of one steady flow computation, multiplied by number of temporal modes desired. For inviscid flows, Hall and Clark demonstrated reasonable accuracy and a speedup of one to two orders of magnitude.

When considering viscous cases however, the amplitude of unsteady phenomena is considerable and linearization errors may be large. To accommodate those effects, Hall et al. [44] introduced the fully non-linear harmonic balance for Euler and Navier-Stokes equations. McMullen et al. [45, 46] also proposed an alternative scheme named the non-linear frequency domain method (NLFD) where the flow equations are solved in the Fourier space directly. The latter is realized in a pseudo-spectral fashion where real and Fourier space information is exchanged through fast-Fourier transform. McMullen et al. also presented the gradient based variable time period method (GBVTP), an adaptive algorithm for flows where the time period is unknown *a-priori*. Similarly to other spectral time representations, the NLFD exhibits remarkable accuracy characteristics. Indeed, by employing the spectral space, the NLFD inherits the exponential convergence of Fourier series. This remarkable feature is numerically demonstrated by Nadarajah [47] for transonic viscous cases.

More recently, Gopinath and Jameson [48] have presented the time spectral (TS) method as an alternative to the NLFD scheme. The TS method eliminates the explicit use of fast Fourier transforms (FFT) in the computation by coupling the real space time instances with a pre-multiplied Fourier collocation matrix. The GBVTP method was also incorporated in the framework [49]. The researchers demonstrated spectral accuracy, but concluded that a high-order spatial discretization is required to reap the full benefits of the fast convergence of Fourier series.

1.3 Objectives of this Research

The aim of this research is to create an efficient and accurate computational method for compressible periodic flows. Indeed, traditional numerical schemes show severe limitations when applied to strongly non-linear unsteady flows, such as those encountered in rotorcraft simulation. For that reason, the challenges presented by these cases motivate the development of more specialized methodologies, tailored to cope with complex flow features and unsteady phenomena.

To this intent, a novel, alternative simulation strategy is presented in this thesis. A numerical framework is developed to solve the inviscid flow equations possessing periodic solutions. The framework's objective is to obtain an improved accuracy level while reducing the computational cost inherent to time-dependent simulations. To achieve this goal, a high-order spectral difference (SD) scheme is combined with a non-linear frequency domain (NLFD) solver. The advantageous numerical properties of these schemes are complementary and ensure high-order accuracy in both time and space, allowing the computation of detailed flow solutions. Furthermore, employing the NLFD spectral temporal representation incorporates directly the periodicity of the solution within the framework, permitting an efficient treatment of the unsteady effects.

The work performed can be split into two categories. One consists in the implementation and validation of a steady SD solver. The other concerns the incorporation of the NLFD method in the SD code. The different milestones and subtasks of the project are presented below.

Implementation of the 2D Spectral Difference solver

- Implement the SD solver.

- Validate the accuracy of the scheme on various test cases.
- LU-SGS for acceleration of steady solutions.

Incorporation of the NLFD method

- Augment the SD solver with an NLFD temporal representation.
- Adapt the LU-SGS to the NLFD framework.
- Validate the temporal scheme and solution procedure.
- Demonstrate the approach for periodic flow problems.

My contributions arising from this investigation are summarized by two novel ideas. First, the use of a Fourier space time representation in conjunction with a high-order spatial discretization. A unified formulation is derived, and the high-order accuracy of the method is demonstrated in both space and time. Second, the efficient solution of the discretized system using a fast, implicit solver. A lower-upper symmetric Gauss-Seidel (LU-SGS) procedure for the NLFD equations is derived and an innovative treatment of the unsteady source term equation (3.39) and Fourier space Jacobian equation (3.44) is presented. The approach is validated, and offers a drastic improvement over the explicit methods used by previous researchers. Ultimately, the developed algorithm should constitute an attractive new avenue for large scale time-dependent problems, alleviating the computational cost traditionally associated with such simulations.

This study is divided into three sections. First, the Euler equation, governing the motion of compressible inviscid fluids are derived from first principles. The subsequent reformulation of those equations allowing their numerical solution is also presented. Secondly the mathematical formulation forming the building blocks of the NLFD-SD scheme are explained. All the numerical methods used in the scheme or in its validation are derived. Lastly multiple test cases are performed to validate and benchmark the proposed algorithm.

CHAPTER 2
The Euler Equations

This chapter presents the complete derivation of the Euler equations for inviscid, compressible fluids. In section 2.1, the fundamental concepts of mass, momentum and energy conservation are applied to obtain a rigorous mathematical model. The resultant system of integral equations is then manipulated and a formulation suitable to the computation of periodic flow problems is presented in section 2.2.

2.1 Integral Form of the Euler Equations

In this section, the conservation law for mass, momentum and energy are derived. For the sake of the discussion, we will consider a control volume Ω, denote its surface $\partial\Omega$, the unit vector pointing in the normal direction $\vec{n}$, and characterize the flow by its velocity $\vec{v}$. The governing equations will arise from the flux balance over that control volume.

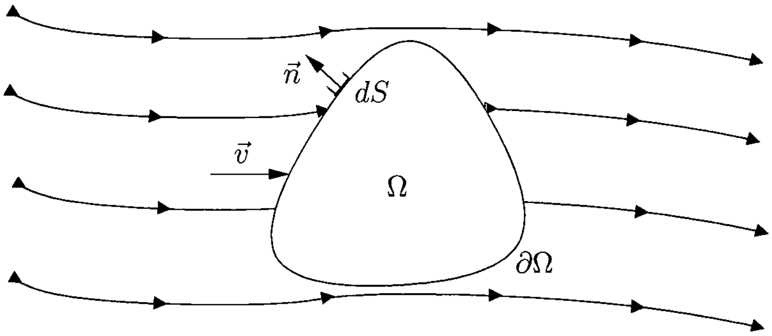

Figure 2–1: Definition of a control volume

2.1.1 Conservation of Mass

The law of mass conservation states that inside a control volume Ω, no mass can be created or destroyed. The time rate of change of the total mass inside that control volume may be expressed using the density ρ as

$$\frac{\partial}{\partial t}\int_{\Omega}\rho \, d\Omega. \tag{2.1}$$

The mass exchanged trough the boundary of the control volume is obtained as a product of the density, area and normal convective velocity. Consequently, the mass flux across a infinitesimal boundary segment dS is

$$\rho \, (\vec{v}.\vec{n}) \, dS. \tag{2.2}$$

Since no source terms or diffusion effects are considered, then the mass conservation equation is the balance between the accumulation term and mass flux across the boundary

$$\frac{\partial}{\partial t}\int_{\Omega}\rho \, d\Omega + \oint_{\partial\Omega}\rho \, (\vec{v}.\vec{n}) \, dS = 0. \tag{2.3}$$

2.1.2 Conservation of Momentum

The equation concerning the conservation of momentum is obtained by applying Newton's second law. It is stated that a change in momentum is caused by the net force acting on a mass element. The rate of change of momentum $\rho\vec{v}$ in the control volume is given by

$$\frac{\partial}{\partial t}\int_{\Omega}\rho\vec{v} \, d\Omega. \tag{2.4}$$

The momentum flux across an infinitesimal boundary segment is obtained as a product of the transported quantity $\rho\vec{v}$, the area and the normal convective velocity.

$$\rho\vec{v} \, (\vec{v}.\vec{n}) \, dS. \tag{2.5}$$

Finally, the change in momentum is caused by forces acting on the mass element. In the Euler equations, the gravitational and viscous effects are neglected, hence the only net force is due to the pressure imposed on the control volume

$$p.\vec{n}\, dS. \tag{2.6}$$

The balance of the accumulation, momentum flux and pressure terms lead to:

$$\frac{\partial}{\partial t}\int_{\Omega} \rho\vec{v}\, d\Omega + \oint_{\partial\Omega} \rho\vec{v}\,(\vec{v}.\vec{n})\, dS + \oint_{\partial\Omega} p\,\vec{n}\, dS = 0. \tag{2.7}$$

2.1.3 Conservation of Energy

The equation concerning the conservation of energy is derived from the first law of thermodynamics. Any change in the total energy in the control volume is created from the work acting on the volume, or net heat flux into it. The total energy of a fluid E is obtained as the sum of its internal energy per unit mass e and its kinetic energy

$$E = e + \frac{1}{2}\,|\vec{v}|^2. \tag{2.8}$$

In the control volume, the total energy per unit volume ρE is conserved; its time variation being given by

$$\frac{\partial}{\partial t}\int_{\Omega} \rho E\, d\Omega. \tag{2.9}$$

The total energy flux trough a boundary segment reads:

$$\rho E\,(\vec{v}.\vec{n})\, dS. \tag{2.10}$$

Finally the work done on the control volume is only due to pressure since viscous effects are neglected. On the boundary this reads

$$p\,(\vec{v}.\vec{n})\, dS. \tag{2.11}$$

The balance of the accumulation, total energy flux and work done on the control volume terms leads to:

$$\frac{\partial}{\partial t}\int_{\Omega} \rho E \, d\Omega + \oint_{\partial\Omega} \rho E \, (\vec{v}.\vec{n}) \, dS + \oint_{\partial\Omega} p \, (\vec{v}.\vec{n}) \, dS = 0. \tag{2.12}$$

2.1.4 Pressure closure

The Euler equations are well-posed only if a closure equation for the pressure is provided. This relationship is obtained by assuming an ideal gas obeying the following equation of state

$$p = \rho R T, \tag{2.13}$$

and considering the general relation between total entalpy H, total energy and pressure

$$H = h + \frac{|\vec{v}|^2}{2} = E + \frac{p}{\rho}. \tag{2.14}$$

Using the definitions $R = c_p - c_v$, $\gamma = c_p/c_v$ and the enthalpy relation for a perfect gas $h = c_p T$, one obtains

$$p = (\gamma - 1)\rho \left(E - \frac{|\vec{v}|^2}{2} \right). \tag{2.15}$$

2.2 Differential Form of the Euler Equations

From a computational standpoint, it is more efficient to gather equations (2.3), (2.7) and (2.12) and treat the Euler equations in the following vector form

$$\frac{\partial}{\partial t}\int_{\Omega} w \, d\Omega + \oint_{\partial\Omega} \vec{F}.\vec{n} \, dS = 0, \tag{2.16}$$

where w is the vector of conserved variables and $\vec{F}$ is the inviscid flux vector. In our computational framework, the motion of solid bodies will be represented using a Lagrangian approach. Consequently, for unsteady cases the inviscid flux vector is modified to account for the grid velocity $\vec{b}$.

$$\vec{F}^M = \vec{F} - \vec{b}\,w. \tag{2.17}$$

Considering the motion of the grid and applying Gauss' divergence theorem, equation (2.16) becomes

$$\int_\Omega \frac{\partial w}{\partial t} + \nabla.\vec{F}^M \, d\Omega = 0. \tag{2.18}$$

The integral relationship (2.18) must hold for any control volume Ω, implying that the integrand is null. Thus, the Euler equations in differential form are

$$\frac{\partial w}{\partial t} + \nabla.\vec{F}^M = 0, \tag{2.19}$$

where w is the vector of conserved variables and $\vec{F}^M = (f, g)$ are the inviscid flux vectors, given by

$$w = \left\{ \begin{array}{c} \rho \\ \rho u \\ \rho v \\ \rho E \end{array} \right\}, \; f = \left\{ \begin{array}{ll} \rho(u - b_x) & \\ \rho u(u - b_x) & +p \\ \rho v(u - b_x) & \\ \rho E(u - b_x) & +pu \end{array} \right\}, \; g = \left\{ \begin{array}{ll} \rho(v - b_y) & \\ \rho u(v - b_y) & \\ \rho v(v - b_y) & +p \\ \rho E(v - b_y) & +pv \end{array} \right\}. \tag{2.20}$$

Here, b_x and b_y are the cartesian grid velocities and p is computed using (2.15).

CHAPTER 3
Computational framework

This chapter presents the proposed non-linear frequency domain-spectral difference scheme for the periodic Euler equations. Section (3.1) presents the formulation and implementation of the spectral difference (SD) spatial discretization. Section (3.2) describing the temporal discretizations used in this work is separated in two parts. Firstly, the explicit and implicit time-accurate integration strategies used for validation purposes are presented, then the NLFD time spectral method is discussed.

3.1 Spectral Difference Spatial Discretization

The basis for the spectral difference solver of order k is a superposition of two grids within each computational cell. Their arrangement within the reference element spanning $(\xi, \eta) \in [-1, 1] \times [-1, 1]$ is illustrated on Fig. (3–1). This particular choice corresponds to the Chebysev-Gauss-Lobbato basis, and the staggered-grid multidomain formulation of Kopriva [35, 36] is recovered. The first grid holds the conserved variables and is chosen such that a polynomial solution of degree $k-1$ may be supported. The coordinates of those so-called *solution points* are given by the Gauss-Chebyschev quadrature points

$$\chi_s = \cos\left(\pi \frac{2s-1}{2k}\right), \quad s = 1, 2, \ldots, k. \tag{3.1}$$

Similarly, the fluxes are computed on a second grid supporting a polynomial of degree k. Those *flux points* are given by the Gauss-Lobatto points

$$\chi_{s+1/2} = \cos\left(\pi \frac{s}{k}\right), \quad s = 0, 1, \ldots, k. \tag{3.2}$$

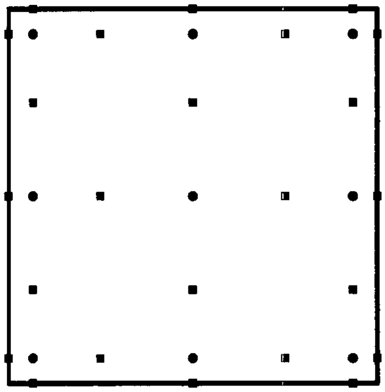

Figure 3–1: Solution (•) and flux (■) points for the third-order SD scheme

Once the nodal placement is defined, Lagrange polynomials are introduced to create an interpolation basis

$$h_i(\chi) = \prod_{s=1,s\neq i}^{k} \left(\frac{\chi - \chi_s}{\chi_i - \chi_s} \right), \tag{3.3}$$

$$l_{i+1/2}(\chi) = \prod_{s=0,s\neq i}^{k} \left(\frac{\chi - \chi_{s+1/2}}{\chi_{i+1/2} - \chi_{s+1/2}} \right). \tag{3.4}$$

The product of those Lagrange polynomials in each spatial direction define the shape functions $\phi(\xi,\eta)$ used to interpolate the discrete solution within the cell.

$$w(\xi,\eta) = \{\phi\}^T \{w\}, \quad (\xi,\eta) \in [-1,1], \tag{3.5}$$

where

$$\phi_{i,j}(\xi,\eta) = h_i(\xi).h_j(\eta). \tag{3.6}$$

In a similar manner, we introduce the shape functions $\varphi(\xi,\eta)$ and $\psi(\xi,\eta)$ for interpolating the fluxes in the ξ and η direction respectively.

$$\varphi_{i,j}(\xi,\eta) = l_{i+1/2}(\xi).h_j(\eta), \tag{3.7}$$

$$\psi_{i,j}(\xi,\eta) = h_i(\xi).l_{j+1/2}(\eta). \tag{3.8}$$

With the basis function defined, the SD scheme can be summarized with the following four steps:

I. Interpolate w from the solution to the flux points.

II. Calculate the discrete flux vector $\vec{F} = (f, g)$ at each flux point.

III. Calculate $\nabla.\vec{F}$ using the derivatives of the flux polynomial.

IV. Advance the solution forward in time.

Step I is achieved by multiplying the discrete solution values by the appropriate basis function, as expressed by (3.5). Step II consist of evaluating the flux vector at each flux point. At the inner points, the solution is continuous and the analytical expression for the flux vector is used. At the boundary however, the solution is allowed to be discontinuous from one cell to another. For this reason, a Riemann solver is used to retrieve a stable, single-valued normal flux. In our implementation, the Rusanov [50] and Roe [51] fluxes are available and are computed as

$$\begin{aligned} f_n^{\text{RUSANOV}} &= \frac{1}{2}[f_n^L + f_n^R - (|v_n - b| + c)(w^R - w^L)], \qquad (3.9) \\ f_n^{\text{ROE}} &= \frac{1}{2}[f_n^L + f_n^R - R|\Lambda|R^{-1}(w^R - w^L)], \qquad (3.10) \end{aligned}$$

where c is the speed of sound, b the mesh velocity, R the right eigenvector matrix and $|\Lambda|$ the entropy-fixed absolute eigenvalues. In the SD scheme, the tangential flux is also required and can be either evaluated locally and left discontinuous, or averaged across the boundary. In this work, the first option is chosen. In practice, the treatment of this tangential component seems to be of minor importance [39]. Finally the full flux vector $\vec{F} = (f, g)$ can be reconstructed by rotating the normal and tangential components to the Cartesian coordinates.

$$\begin{cases} f = n_x\, f_n + t_x\, f_t \\ g = n_y\, f_n + t_y\, f_t \end{cases} \qquad (3.11)$$

Step III consists of constructing a polynomial from the discrete flux values and taking its derivatives to form the flux divergence. This is done in one single step by using the derivative of the basis function φ and ψ. For example, the f flux is interpolated from the discrete values $\{f\}$ by

$$f(\xi,\eta) = \{\varphi\}^T\{f\} \quad \xi\text{-direction}, \tag{3.12}$$

$$f(\xi,\eta) = \{\psi\}^T\{f\} \quad \eta\text{-direction}. \tag{3.13}$$

Therefore its spatial derivatives are

$$f_\xi(\xi,\eta) = \{\varphi_\xi\}^T\{f\}, \tag{3.14}$$

$$f_\eta(\xi,\eta) = \{\psi_\eta\}^T\{f\}. \tag{3.15}$$

As the reconstruction is universal for all the cells of the domain, the values of φ_ξ and ψ_η at the solution points are computed in a pre-processing step for the reference element only. The derivatives of the g flux is treated in the same manner. Finally, applying the chain rule, we can obtain the divergence of the fluxes in physical space using the appropriate metric terms given in appendix A

$$\nabla.\vec{F} = \frac{\partial f}{\partial \xi}\xi_x + \frac{\partial f}{\partial \eta}\eta_x + \frac{\partial g}{\partial \xi}\xi_y + \frac{\partial g}{\partial \eta}\eta_y, \tag{3.16}$$

or in terms of the discrete nodal values

$$\nabla.\vec{F} = \xi_x\{\varphi_\xi\}^T\{f\} + \eta_x\{\psi_\eta\}^T\{f\} + \xi_y\{\varphi_\xi\}^T\{g\} + \eta_y\{\psi_\eta\}^T\{g\}. \tag{3.17}$$

The formulas for the metric terms ξ_x, ξ_y, η_x, and η_y are given in appendix A. By defining the residual operator as the discrete flux divergence, the SD discretization results in a set of ordinary differential equations, expressed as

$$\frac{\partial w}{\partial t} + R(w) = 0. \tag{3.18}$$

The step IV consisting of marching the solution in time is achieved by applying the method of lines. Indeed, the discretization reduced the system of partial differential equation to a set of coupled ordinary differential equations and any standard integration scheme can be applied to solve (3.18). The different approaches used in this work are presented in section (3.2).

Some precautions must be taken when mapping operations from physical to computational space. Indeed, it is well known that high-order methods are particularly sensitive to the representation of curved boundaries [24, 30, 39]. For that purpose, cells with quadratic edges are used to accommodate the curvature of solid walls. This is realized by adding a node to each segment representing a curved surface, then using the resulting high-order metrics. In this research, this additional node is obtained through a globally interpolated B-Spline. Bassi [24] reports that the improvement due to high-order boundaries is mainly related to the correct distribution of the normal vectors. To take this into account, the normal vectors are computed from the analytical derivatives of the fitted B-Spline. All the airfoil simulations to be presented have benefited from this high-order boundary approach.

3.2 Temporal Discretization

This section presents the various computational methods used to treat the temporal evolution of the solution. Firstly, the explicit Runge-Kutta scheme used in this work is described in subsection (3.2.1). Secondly, the lower-upper symmetric Gauss-Seidel used to accelerate the convergence of steady problem is derived in subsection (3.2.2). Thirdly, a second-order dual-time stepping scheme is formulated in subsection (3.2.3). Lastly, the NLFD approach is presented in subsection (3.2.4), where the emphasis is put on the solution procedure and the integration within the complete NLFD-SD scheme.

3.2.1 Explicit Runge-Kutta

In this work, explicit computations are realized using a multistep Runge-Kutta (RK5) scheme. Equation (3.18) is integrated from time level n to time level $n+1$ by letting $i = 1 \to 5$.

$$\begin{aligned} w^0 &= w^n, \\ w^{i+1} &= w^n - \alpha_i \, \Delta t \; R(w^i), \\ w^{n+1} &= w^5. \end{aligned} \tag{3.19}$$

For unsteady problems, we seek to maximize the accuracy and coefficients providing second-order accuracy [52] are used.

$$\alpha_1 = 1/4,\ \alpha_2 = 1/6,\ \alpha_3 = 3/8,\ \alpha_4 = 1/2,\ \alpha_5 = 1. \tag{3.20}$$

For steady problems, the order of the integration scheme does not play a role in the final steady-state solution. Consequently, we adopt the modified stage coefficients given by Van Leer [53], trading formal accuracy for an enlarged stability region. Our numerical experiments have shown that the time step restriction is favorably relaxed.

$$\alpha_1 = .0695,\ \alpha_2 = 0.1602,\ \alpha_3 = 0.2898,\ \alpha_4 = 0.5060,\ \alpha_5 = 1. \tag{3.21}$$

3.2.2 Lower-Upper Symmetric Gauss-Seidel

To accelerate the convergence to steady-state, Sun et al. [54] have introduced the lower-upper symmetric Gauss-Seidel (LU-SGS) solution algorithm for the SD scheme. Being based on a backward Euler discretization of the temporal derivative, it is theoretically unconditionally stable, and first-order accurate. The main advantage of the LU-SGS is that the degrees of freedom of the solution are solved in a coupled manner by sweeping through the domain rather than solving a linear system. Due to this unique feature, the LU-SGS presents the efficiency associated with implicit schemes without the associated memory penalty.

The derivation starts with the equations in semi-discrete ODE form (3.18), which are discretized using the Euler backward formula. For each cell c, we write

$$\frac{w_c^{n+1} - w_c^n}{\Delta t} + \left[R_c(w^{n+1}) - R_c(w^n)\right] \;=\; -R_c(w^n). \tag{3.22}$$

We linearize the residual, distinguishing between the cell's and the neighbor's contributions

$$\frac{w_c^{n+1} - w_c^n}{\Delta t} + \frac{\partial R_c}{\partial w_c}\left[w_c^{n+1} - w_c^n\right] + \sum_{nb \neq c} \frac{\partial R_c}{\partial w_{nb}}\left[w_{nb}^{n+1} - w_{nb}^n\right] \;=\; -R_c(w^n). \tag{3.23}$$

To accelerate the convergence to steady-state, the scheme employs a Gauss-Seidel approach where the latest available solution is used. This allows to transfer the neighbor's contribution to the right-hand side. Noting by '$*$' the latest available update, we write

$$\frac{w_c^{n+1} - w_c^n}{\Delta t} + \frac{\partial R_c}{\partial w_c}\left[w_c^{n+1} - w_c^n\right] \;=\; -\sum_{nb \neq c} \frac{\partial R_c}{\partial w_{nb}}\left[w_{nb}^{n+1} - w_{nb}^n\right]^* - R_c(w^n). \tag{3.24}$$

The equation (3.24) will be solved iteratively. Noting 's' the sweep iteration and factorizing the left-hand-side (LHS) leads to

$$\left(\frac{I}{\Delta t} + \frac{\partial R_c}{\partial w_c}\right)\left[w_c^{n+1} - w_c^n\right]^{s+1} \;=\; -\sum_{nb \neq c} \frac{\partial R_c}{\partial w_{nb}}\left[w_{nb}^{n+1} - w_{nb}^n\right]^* - R_c(w^n). \tag{3.25}$$

It is possible to further simplify the scheme by approximating the neighboring cell's contributions. Using first order Taylor approximations, the right-hand-side (RHS) of (3.25) is modified in the following fashion

$$\begin{aligned} RHS &= -\sum_{nb\neq c} \frac{\partial R_c}{\partial w_{nb}} \left[w_{nb}^{n+1} - w_{nb}^{n}\right]^* - R_c(w_c^n, w_{nb}^n), \\ &\approx -R_c(w_c^n, w_{nb}^*), \\ &\approx -R_c(w_c^*, w_{nb}^*) + \frac{\partial R_c}{\partial w_c}\left[w_c^{n+1} - w_c^n\right]^*, \\ &= -R_c(w^*) + \frac{\partial R_c}{\partial w_c}\left[w_c^{n+1} - w_c^n\right]^s. \end{aligned} \tag{3.26}$$

We obtain (3.26) since the latest available update term $[w_c^{n+1} - w_c^n]^*$ for cell c is necessarily the one computed at the previous sweep level. A remarkable fact is that the off-diagonal blocks $\partial R_c/\partial w_{nb}$ have disappeared from the formulation, reducing considerably the storage requirements.The simplified RHS is replaced in equation (3.25)

$$\left(\frac{I}{\Delta t} + \frac{\partial R_c}{\partial w_c}\right)\left[w_c^{n+1} - w_c^n\right]^{s+1} = -R_c(w^*) + \frac{\partial R_c}{\partial w_c}\left[w_c^{n+1} - w_c^n\right]^s. \tag{3.27}$$

Finally, the scheme is manipulated to find

$$\left(\frac{I}{\Delta t} + \frac{\partial R_c}{\partial w_c}\right)\left[w_c^{n+1,s+1} - w_c^{n+1,s}\right] = -R_c(w^*) - \frac{\left[w_c^{n+1} - w_c^n\right]^s}{\Delta t}, \tag{3.28}$$

where $[w_c^{n+1} - w_c^n]^s$ can be viewed as an approximate Newton step as Δt tends to infinity, and where $[w_c^{n+1,s+1} - w_c^{n+1,s}]$ is its update computed from the sweeping process. Equation (3.28) is solved for each cell using a lower-upper factorization until the time-step is sufficiently converged.

3.2.3 Dual Time Stepping

A popular approach for time dependent computations is to employ the second-order backward difference formula (BDF2) as a base to the implicit discretization. In that case, the semi-discrete scheme (3.18) becomes

$$\frac{3w^{n+1} - 4w^n + w^{n-1}}{2\Delta t} = -R(w^{n+1}). \tag{3.29}$$

One approach to solve equation (3.29) is employing a dual-time stepping strategy. An unsteady residual gathering the time terms and the original residual is defined as

$$R^\star = \frac{3w^\star - 4w^n + w^{n-1}}{2\Delta t} + R(w^\star), \tag{3.30}$$

where $w^\star$ is an approximation to w^{n+1}. As a consequence, each time step consists of solving the following steady problem in pseudo-time

$$\frac{\partial w^\star}{\partial \tau} = -R^\star. \tag{3.31}$$

At convergence, the pseudo-time derivative vanishes and $w^\star = w^{n+1}$. In our implementation, the LU-SGS scheme described in section (3.2.2) is used to efficiently solve the inner iterations. In addition, further improvements are obtained by initializing the iteration with the following extrapolated estimate

$$w^\star_{\text{guess}} = w^n + \frac{3w^n - 4w^{n-1} + w^{n-2}}{\Delta t}. \tag{3.32}$$

3.2.4 Non-Linear Frequency Domain

In contrast with the other techniques presented, the non-linear frequency domain (NLFD) method is specialized to the class of problems with periodic solutions. One period of the flow evolution is decomposed into different discrete time instances. Each of those discrete flow "snapshots" are then assembled together in Fourier space where the harmonic content of the flow is determined.

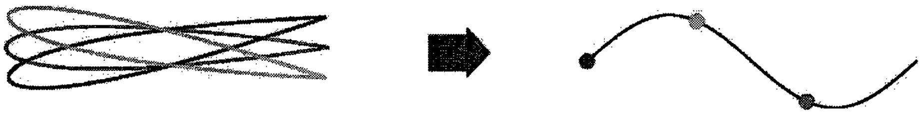

Figure 3–2: NLFD conceptual sketch

Using the periodicity assumption, the state vector w and residual R may be represented by separate Fourier series:

$$w = \sum_{k=-\frac{N}{2}}^{\frac{N}{2}} \hat{w} e^{ikt}, \quad R = \sum_{k=-\frac{N}{2}}^{\frac{N}{2}} \hat{R} e^{ikt}, \tag{3.33}$$

where $i = \sqrt{-1}$. Those expressions are replaced in the semi-discrete form (3.18) and using the orthogonality property of the Fourier series, yields a separate equation for each wavenumber k:

$$ik\hat{w}_k + \hat{R}_k = 0. \tag{3.34}$$

To solve the above equation a pseudo-time derivative is added, and the resulting equations are integrated to steady state, at which point (3.34) is satisfied.

$$\frac{d\hat{w}_k}{d\tau} + ik\hat{w}_k + \hat{R}_k = 0. \tag{3.35}$$

In the original implementation by McMullen et al. [45, 46, 55], integration to steady-state is done using a multistage Runge-Kutta method. For comparison purposes, we have employed the five-stage scheme presented in section (3.2.1). The application to the NLFD equations gives

$$\begin{aligned} \hat{w}_k^0 &= \hat{w}_k^n, \\ \hat{w}_k^{i+1} &= \hat{w}_k^n - \alpha_i \, \Delta\tau \, \hat{R}^\star(\hat{w}_k^i), \\ \hat{w}_k^{n+1} &= \hat{w}_k^5. \end{aligned} \tag{3.36}$$

where $\hat{R}^\star(\hat{w}_k) = -ik\hat{w}_k - \hat{R}_k$ and the coefficients α_i are given by (3.21).

A faster rate of convergence may be obtained by replacing the multistep integration by an implicit technique. For that purpose, we adapt Sun et al.'s [54] implicit LU-SGS method, presented in section (3.2.2). As previously stated, the NLFD solution strategy implies driving to steady-state each modal equation (3.35). However, the

Fourier coefficients $\hat{w}_k$ and $\hat{R}_k$ are complex numbers, thus creating an equation for both real and imaginary parts

$$\frac{\partial \hat{w}_{\mathbf{R}}}{\partial \tau} + \hat{R}_{\mathbf{R}} - k\hat{w}_{\mathbf{I}} = 0, \tag{3.37}$$

$$\frac{\partial \hat{w}_{\mathbf{I}}}{\partial \tau} + \hat{R}_{\mathbf{I}} + k\hat{w}_{\mathbf{R}} = 0. \tag{3.38}$$

Since these equations are coupled through the source term $ik\hat{w}_k$, a fully implicit scheme would require to solve them simultaneously. To preserve the simplicity of the original NLFD method, we keep this source term explicit, allowing us to solve the real and imaginary parts separately. For each cell, we write

$$\frac{\hat{w}_c^{n+1} - \hat{w}_c^n}{\Delta\tau} + \left[\hat{R}_c^{n+1} - \hat{R}_c^n\right] = -\hat{R}_c^n - ik\hat{w}_c^n. \tag{3.39}$$

We linearize the residual, distinguishing between the cell's and the neighbor's contributions

$$\frac{\hat{w}_c^{n+1} - \hat{w}_c^n}{\Delta\tau} + \frac{\partial \hat{R}_c}{\partial \hat{w}_c}\left[\hat{w}_c^{n+1} - \hat{w}_c^n\right] + \sum_{nb\neq c} \frac{\partial \hat{R}_c}{\partial \hat{w}_{nb}}\left[\hat{w}_{nb}^{n+1} - \hat{w}_{nb}^n\right] = -\hat{R}_c^n - ik\hat{w}_c^n. \tag{3.40}$$

Next, we apply the Gauss-Seidel and noting by 's' the sweep iteration and by '$*$' the latest available update

$$\left(\frac{I}{\Delta\tau} + \frac{\partial \hat{R}_c}{\partial \hat{w}_c}\right)\left[\hat{w}_c^{n+1} - \hat{w}_c^n\right]^{s+1} = -\sum_{nb\neq c} \frac{\partial \hat{R}_c}{\partial \hat{w}_{nb}}\left[\hat{w}_{nb}^{n+1} - \hat{w}_{nb}^n\right]^* - \hat{R}_c^n - ik\hat{w}_c^n. \tag{3.41}$$

It is possible to further simplify the scheme by approximating the neighboring cell's contributions

$$\begin{aligned} RHS &= -\hat{R}_c(w_c^n, w_{nb}^n) - \sum_{nb\neq c} \frac{\partial \hat{R}_c}{\partial \hat{w}_{nb}}\left[\hat{w}_{nb}^{n+1} - \hat{w}_{nb}^n\right]^* \\ &\approx -\hat{R}_c(w_c^n, w_{nb}^*) \\ &\approx -\hat{R}_c(w_c^*, w_{nb}^*) + \frac{\partial \hat{R}_c}{\partial \hat{w}_c}\left[\hat{w}_c^{n+1} - \hat{w}_c^n\right]^* \\ &= -\hat{R}_c^* + \frac{\partial \hat{R}_c}{\partial \hat{w}_c}\left[\hat{w}_c^{n+1} - \hat{w}_c^n\right]^s . \end{aligned} \tag{3.42}$$

Using this approximation, the scheme simplifies to

$$\left(\frac{I}{\Delta\tau}+\frac{\partial\hat{R}_c}{\partial\hat{w}_c}\right)\left[\hat{w}_c^{n+1,s+1}-\hat{w}_c^{n+1,s}\right] \quad = \quad -\left(\hat{R}_c^{*}+\frac{\left[\hat{w}_c^{n+1}-\hat{w}_c^{n}\right]^{s}}{\Delta\tau}+ik\hat{w}_c^{n}\right). \tag{3.43}$$

In the practical implementation of the scheme, the left-hand side matrix of (3.43) is assembled and stored in factorized lower-upper form for the real and imaginary parts of all the modes of each cell, at all discrete time instances. Using a symmetric sweeping pattern, we solve each cell sequentially by doing triangular solves until the time step is deemed sufficiently converged. Since we only require a steady state solution to (3.35), partial convergence of each time step is sufficient and thus, the minimum number of sweeps that guarantees convergence are used. As noted by Fidkowski[56], solution schemes based on a local linearization of the residual can fail if a poor initial guess is used. Indeed, it is possible to predict a negative density or pressure in the early stages of the solution procedure. To prevent such non-physical quantities, a first-order accurate solution is computed and used to initialize the iterative NLFD-SD scheme. The low order operator is significantly less stiff but provides an excellent first guess.

The residual in Fourier space is obtained using a pseudo-spectral approach. A flow period is divided in a number of n distinct time steps where the time dependent real space residual is calculated. Using a discrete Fourier transform, the $(n+1)/2$ first modes of the spectral residual $\hat{R}_k^{*}$ are obtained and used in (3.43). Similarly, w is calculated from $\hat{w}_k$ by using the inverse Fourier transform. Using this pseudo-spectral method also considerably simplifies the computation of the scheme's Jacobian. Indeed, using the chain-rule we have that:

$$\frac{\partial\hat{R}}{\partial\hat{w}}=\sum_{r=1}^{n}\frac{\partial\hat{R}}{\partial R_r}\frac{\partial R_r}{\partial w_r}\frac{\partial w_r}{\partial\hat{w}}, \tag{3.44}$$

where r denotes the time steps in real space. Moreover, noticing that $\partial\hat{R}/\partial R$ and $\partial w/\partial\hat{w}$ are simply the coefficients forming the basis functions of the forward and inverse Fourier transforms, we conclude that the spectral Jacobians are easily calculated as a linear combination of the real space Jacobians. This method is significantly simpler than formally expressing $\hat{R}$ as a function of $\hat{w}$ and taking the appropriate derivatives.

The algorithm of the NLFD-SD scheme is summarized by Fig. (3–3). On this figure, the operations effectuated in real space (time domain) are shown in blue and the Fourier space (frequency domain) operations are in black. The steady-state solution of the equations (3.35) is obtained by sequentially applying the following steps to each cell of the domain:

I. Start with n real space instances w.
II. Use spectral difference discretization to obtain R and $\partial R/\partial w$ for each.
III. Compute $\hat{R}$ and $\partial\hat{R}/\partial\hat{w}$ using discrete Fourier transform.
IV. Compute RHS and retrieve stored LHS.
V. Compute update $\delta\hat{w}^*$ and correct Fourier space coefficients $\hat{w}$ accordingly.
VI. Obtain updated w using inverse discrete Fourier transform.
VII. Move to next cell.

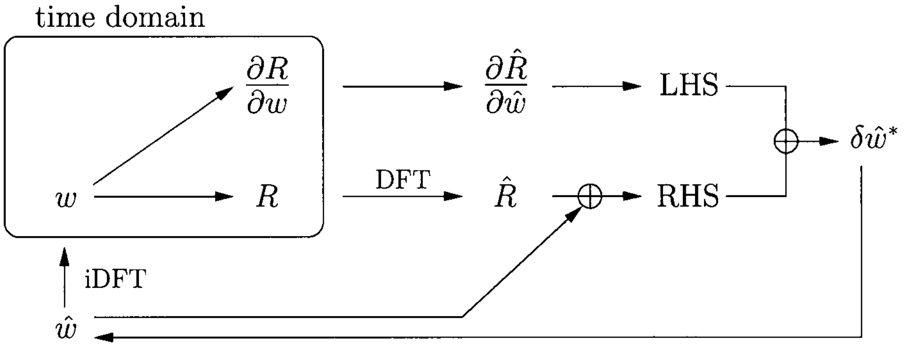

Figure 3–3: NLFD flow chart

3.3 Implementation Details

All the mathematical algorithms presented in this chapter were implemented from scratch, without recycling older code. All the solvers developed were written using Fortran 90 and share the same spectral difference discretization routines. However, it was found easier to have separate codes corresponding to each class of test case. The cases were performed on a computer cluster running the Linux Red Hat Enterprise 3 operating system and consisting of 2.2GHz AMD Operon 248 processing units having 2GB of memory per node. Finally, the grids for the airfoil cases were created using Hyperg, a hyperbolic grid generator written by Prof. Jameson from Stanford university.

CHAPTER 4
Validation

This chapter presents the validation procedure for the NLFD-SD scheme where three cases are considered. Firstly, the spectral-difference implementation is validated on the vortex advection problem in subsection (4.1). This test case is also used to verify the accuracy of the RK5 and LU-SGS time marching schemes. Secondly, subsection (4.2) presents a parametric study where the subsonic flow over an airfoil is considered. Finally the NLFD-SD scheme is demonstrated in subsection (4.3) where the proposed methodology is applied to compute the subsonic flow over an oscillating airfoil.

4.1 Vortex Advection

To numerically evaluate the accuracy of our SD solver, we chose to solve the vortex advection of Shu [18]. In a mean diagonal flow, perturbations in the velocity and temperature fields are added such that an isentropic vortex is created.

$$\begin{aligned}
(\rho, u, v, p) &= (1,1,1,1), && (4.1)\\
(\delta u, \delta v) &= \frac{\varepsilon}{2\pi} e^{\frac{1}{2}(1-r^2)}(-\bar{y}, \bar{x}), && (4.2)\\
\delta T &= -\frac{(\gamma-1)\varepsilon^2}{8\gamma\pi^2} e^{(1-r^2)}, && (4.3)\\
\varepsilon &= 5, && (4.4)
\end{aligned}$$

where $r^2 = \bar{x}^2 + \bar{y}^2$, $\bar{x} = x - 7$, $\bar{y} = y - 7$. If the domain is infinitely large, the Euler equations admit an exact solution that is the passive advection of the original vortex along the mean flow at a mean velocity of (1,1). To replicate this condition, we solve the problem on a computational domain of size $[0,14] \times [0,14]$

with periodic boundaries. This domain is discretized using five uniform structured grids of successive refinements. The coarser grids are generated from the fine grids by eliminating every other point. The numerical fluxes are evaluated using the Roe's [51] Riemann solver. The simulations are integrated to $t = 2$ using the five-stage Runge-Kutta scheme using the coefficient (3.20). The time step was chosen sufficiently small to ensure time step independent solutions where the spatial discretization error dominates. An example of the final solution on the coarsest grid is presented in Fig. (4–1).

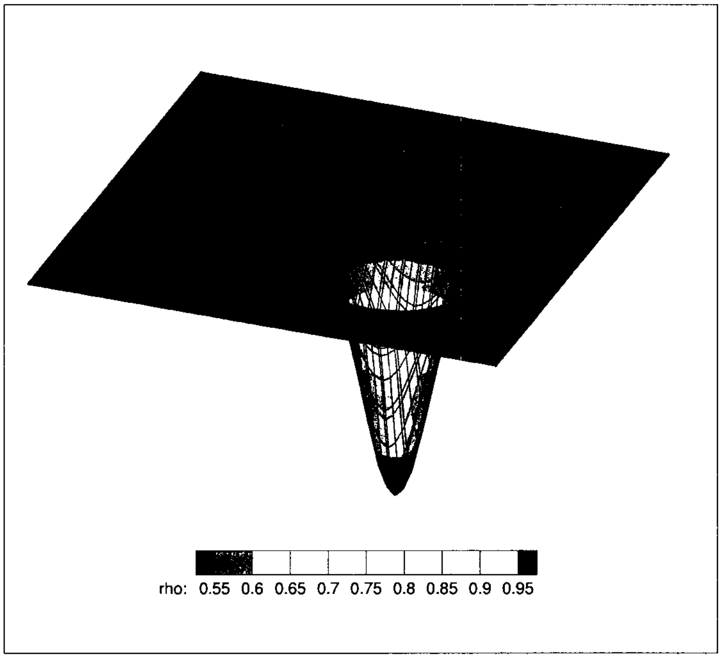

Figure 4–1: Vortex advection problem, 30×30, SD3: solution grid and computed density

To evaluate the level of error in the computed solution, the root-mean-square (RMS) and maximum (MAX) norms are defined based on the density field.

$$e_{\mathrm{MAX}} = \max_i |\rho_i - \rho_{\mathrm{exact}}|, \quad e_{\mathrm{RMS}} = \left(\frac{1}{n} \sum_{i=1}^{n} |\rho_i - \rho_{\mathrm{exact}}|^2 \right)^{1/2}. \tag{4.5}$$

To demonstrate the accuracy of the scheme, numerical simulations are conducted and compared using the first- through fourth-order SD schemes (SD1-SD4). The evolution of the RMS density error as a function of the grid size is presented in Fig. (4–2). As expected, a linear error decay is obtained, where the slope of each line approximates the scheme's order. From this plot, it is deduced that the formal order of convergence is achieved for all four formulations. Fig. (4–3) also presents the measured RMS error as a function of the number of degrees of freedom (DOF) of the solution. It can be noted that for a prescribed number of unknowns, the fourth-order SD scheme yields the lowest level of error, demonstrating the benefits of high-order formulations. Finally, the quantitative data for those simulations is detailed in Table (4–1). A nearly ideal order of accuracy is reported for all simulations in both RMS and MAX errors norms.

To validate the time marching algorithms, the 30×30 third-and fourth-order accurate simulations are repeated using the LU-SGS integration scheme. Figures (4–4) and (4–5) presenting the error as a function of the time step compare the LU-SGS results to those obtained with the RK5 scheme. In the asymptotic range, the error of the LU-SGS simulation decreases linearly with a slope of about one, thereby numerically verifying its formal first-order temporal accuracy. Moreover, the LU-SGS computations also converge to a level of precision similar to the RK5 results once the temporal error is sufficiently decayed. This clearly demonstrates that the implicit formulation preserves the spatial high-order accuracy of the SD scheme. However, being first-order in time, the implicit LU-SGS is much more diffusive and requires smaller time steps than the RK5 method to achieve a converged error level. Since the scheme is destined for steady computations where we use the largest time step possible, this deficiency is of minor importance only.

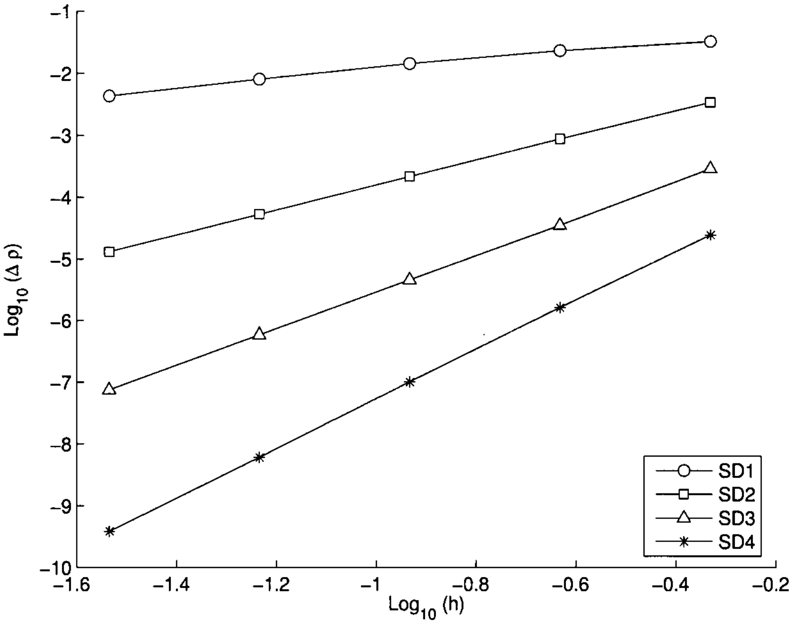

Figure 4–2: Vortex advection problem: Density error as a function of grid size

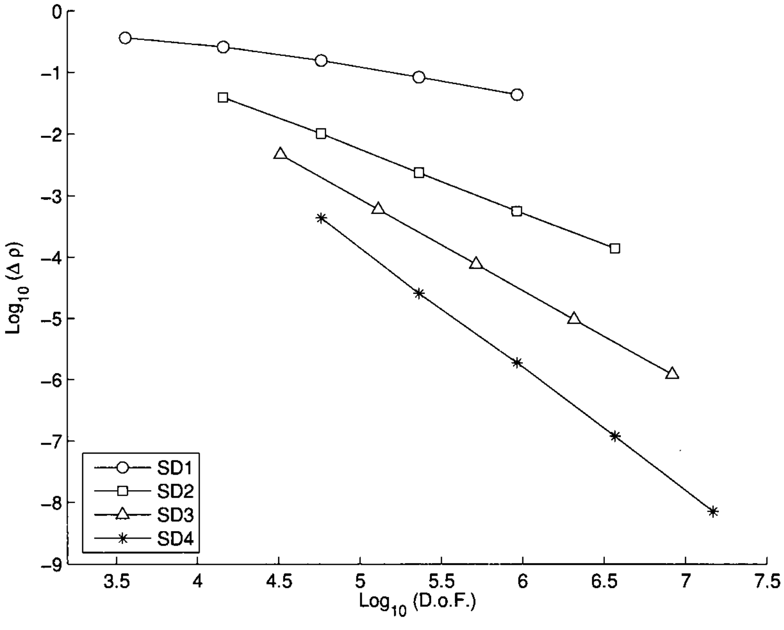

Figure 4–3: Vortex advection problem: Density error as a function of degrees of freedom

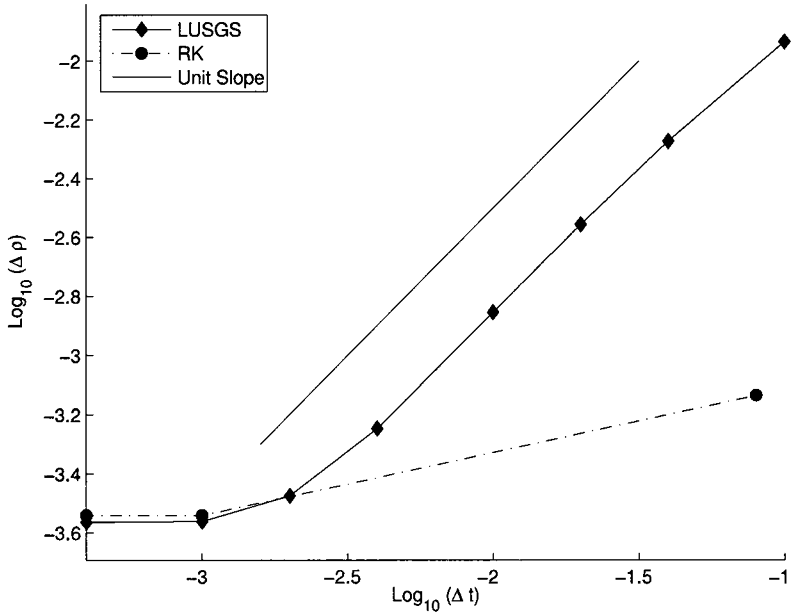

Figure 4–4: Vortex advection problem, 30×30, SD3: Density error as a function of time step

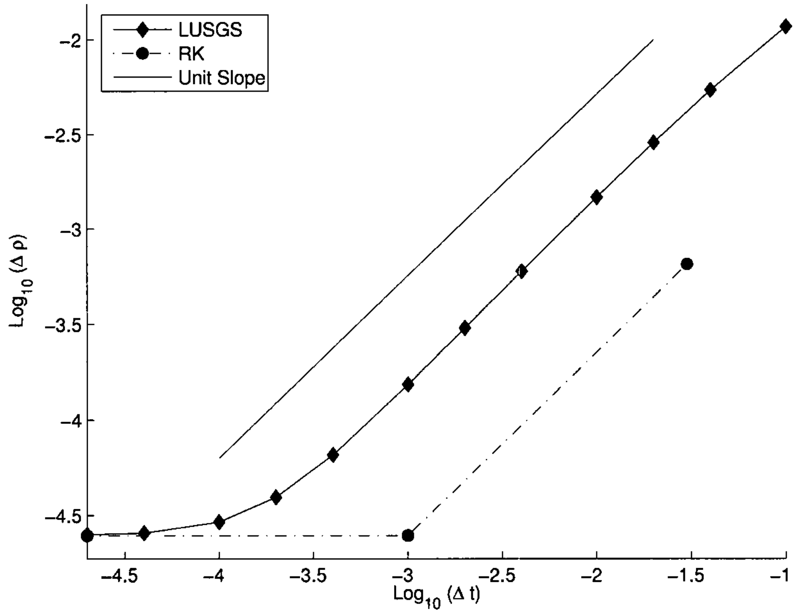

Figure 4–5: Vortex advection problem, 30×30, SD4: Density error as a function of time step

Order	Grid	D.o.f.	RMS error	RMS order	MAX error	MAX order
	30 × 30	3600	.32597e-01	-	.36220e+00	-
	60 × 60	14400	.23076e-01	0.4983	.25648e+00	0.4979
1	120 × 120	57600	.14263e-01	0.6941	.15431e+00	0.7330
	240 × 240	230400	.80307e-02	0.8287	.83311e-01	0.8893
	480 × 480	921600	.42818e-02	0.9073	.43273e-01	0.9450
	30 × 30	14400	.33752e-02	-	.39141e-01	-
	60 × 60	57600	.87539e-03	1.9470	.10222e-01	1.9370
2	120 × 120	230400	.21616e-03	2.0178	.23557e-02	2.1174
	240 × 240	921600	.53175e-04	2.0233	.56093e-03	2.0703
	480 × 480	3686400	.13163e-04	2.0143	.13923e-03	2.0104
	30 × 30	32400	.28735e-03	-	.46465e-02	-
	60 × 60	129600	.35207e-04	3.0289	.59742e-03	2.9593
3	120 × 120	518400	.45436e-05	2.9540	.76179e-04	2.9713
	240 × 240	2073600	.58932e-06	2.9467	.96220e-05	2.9850
	480 × 480	8294400	.75185e-07	2.9705	.12054e-05	2.9968
	30 × 30	57600	.24684e-04	-	.43526e-03	-
	60 × 60	230400	.16228e-05	3.9270	.25705e-04	4.0818
4	120 × 120	921600	.10171e-06	3.9960	.18959e-05	3.7611
	240 × 240	3686400	.60305e-08	4.0760	.12003e-06	3.9814
	480 × 480	14745600	.38354e-09	3.9748	.71053e-08	4.0784

Table 4–1: RMS and MAX density errors and orders of accuracy for the vortex advection problem

4.2 Steady Subsonic Airfoil

To validate the implemented SD solver on a more complex problem involving solid boundaries, a steady airfoil problem is tackled. The second- through fourth-order SD schemes (SD2-SD4) are used to solve the flow around a NACA0012 airfoil in subsonic regime. The freestream Mach number is $M_\infty = 0.5$ and the angle of incidence is $\alpha = 2^o$. All simulations use Roe's [51] numerical flux, a quadratic solid wall representation and a far-field boundary condition based on Riemann invariants with vortex correction. Meshes of size 128×32, 91×20 and 64×16 are used respectively, such as to keep the number of degrees of freedom uniform between the three runs. The time integration is performed using the implicit LU-SGS scheme.

To numerically quantify the solution accuracy, the spurious entropy production is compared. Indeed, it can be shown that the subsonic steady Euler equation are isentropic, thus any deviation from the free stream entropy S_∞ is due to the numerical viscosity introduced by the discretization scheme. As a consequence, the local entropy deviation serves as an elegant error estimator, and can be computed as

$$\Delta S_i = S_i - S_\infty = \left(\frac{p}{\rho^\gamma}\right)_i - 1. \tag{4.6}$$

Similarly, the numerical drag coefficient c_d can be used as an error norm since subsonic inviscid flows follow D'Alembert's paradox and are free of drag.

The computational grids and the resulting pressure contours are shown in Fig. (4–6) through Fig. (4–8). While the second-order solution exhibits oscillations, the high-order solutions are quite smooth and well resolved. Although all simulations have 6.5×10^4 DOF, the high-order solutions appear to be more accurate. Figure (4–9) presents the entropy profile along the airfoil for each solution. The average entropy level in the domain is 9.64×10^{-5}, 3.47×10^{-5} and 1.64×10^{-5} for the second- through fourth-order simulations. Accordingly, the third- and fourth-order schemes represent improvements by a factor of 3 and 6 respectively. The computed drag coefficients for the three simulations are 1.6×10^{-4}, 8×10^{-5} and 6×10^{-5}; predicting a similar trend. The quantitative figures confirm that the high-order SD schemes are less diffusive and the spurious viscosity accounts for less than a drag count (10^{-4}).

Next, the exponential convergence of the SD scheme is explored. To do so, the order of accuracy the scheme is increased while keeping the computational mesh fixed. The very coarse grid utilized is shown in Fig. (4–10 a). The error level corresponding to the first- through fifth-order computations are presented in Fig. (4–10 b). In this figure, the accelerating rate of convergence is clearly visible, indicating that spectral accuracy under p-refinement is achieved even for this relatively complex case. It should be noted that this property was lost for the SD of order six and above. Venkatakrishnan et al. [57] also experienced a similar limitation with high-order finite-element schemes. Those researchers suggested that the slope discontinuity of NACA airfoils' trailing-edge limits the convergence rate of high-order methods. This assertion is consistent with the trailing-edge entropy spike present on Fig. (4–9).

Since this validation case possesses a steady state solution, we will also use it to perform a parametric study of the implicit LU-SGS time stepping scheme. The comparison against the five-stage explicit integration scheme is done using the third-order scheme on the 128×32 grid. Figures (4–11) and (4–12) display a comparison of the explicit and implicit schemes and investigates the effect of time step, number of sweeps, as well as the effect of freezing the Jacobian matrix. Figure (4–11 a) presents the effect of the time step on the convergence of the LU-SGS, the number of symmetric forward and backward sweeps being kept to three. In this figure, the RMS residual is plotted against the wall clock time, given in tenth of a second (1/10 sec). As it can be observed, the implicit method is far more efficient to the explicit method and allows for a CFL number four orders of magnitude larger, and thus converges as much as 27 times faster. The effect of the number of forward and backward Gauss-Seidel sweeps are compared in Fig. (4–11b). The primary motivation is to reduce the number of sweeps to solve approximately each time step, thereby reducing the total computational cost while still ensuring the stability of the scheme. Figure (4–11 b) illustrates that three sweeps is the minimum allowed for this test case, while adding more sweeps slows down the computation. Next, we explore the effect of freezing the Jacobian matrix. In Sun et al.'s [54] paper, it is reported that the performance of the LU-SGS method can be further improved by using a matrix freezing strategy. Indeed, the computation and factorization of the cells' Jacobians is a relatively costly procedure which can be bypassed by using the same matrix for multiple time steps. To this end, the Jacobians are kept frozen once the RMS residual drops below 10^{-2}. Figure (4–12 a) shows the convergence rate for freezing frequencies of 0, 3, 10 and 20 time steps where a 17% improvement over the normal scheme is noticed. Finally, for sake of completeness, the optimal parameters for the LU-SGS are also tested using the other SD formulations on the same grid. Figure (4–12 b) studies the effect of the order of accuracy on the convergence rate, and the RMS residual is plotted against the number of iterations. The first-and second-order schemes exhibits a slightly faster convergence rate due to a higher allowable CFL number; however, both the third-and fourth-order schemes display similar rates.

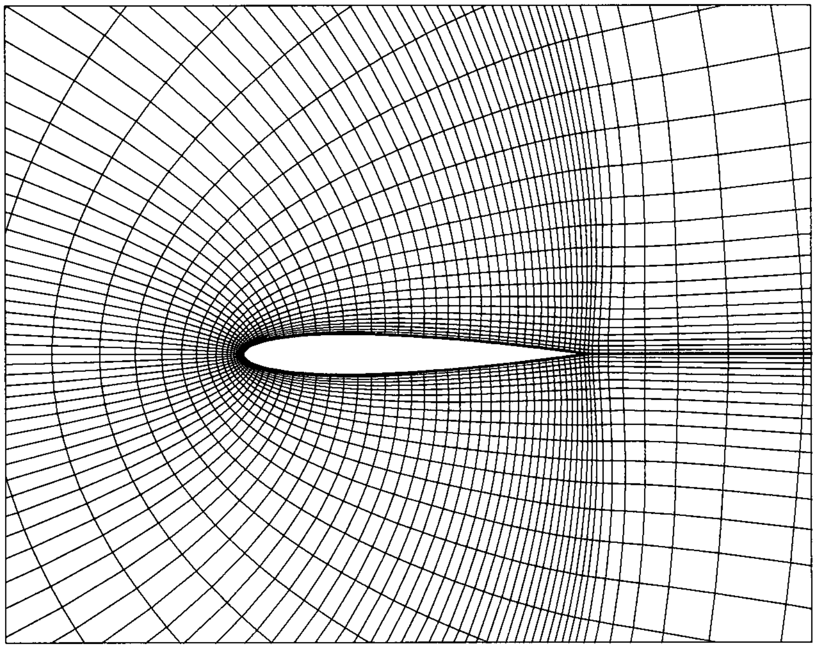

(a) Mesh 128×32

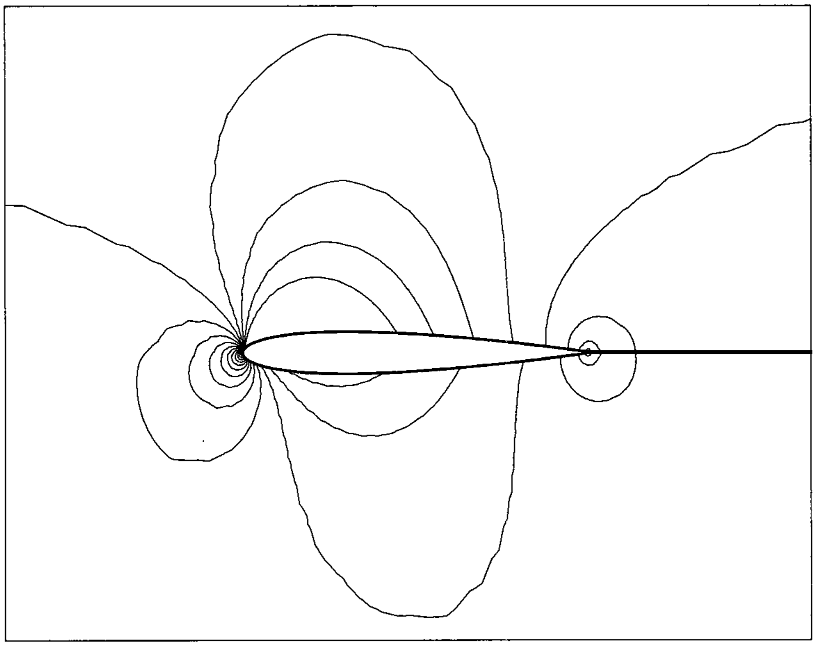

(b) c_p contours, 65536 D.o.f

Figure 4–6: NACA 0012, $M_\infty = 0.5$, $\alpha = 2^o$: Second-order computation

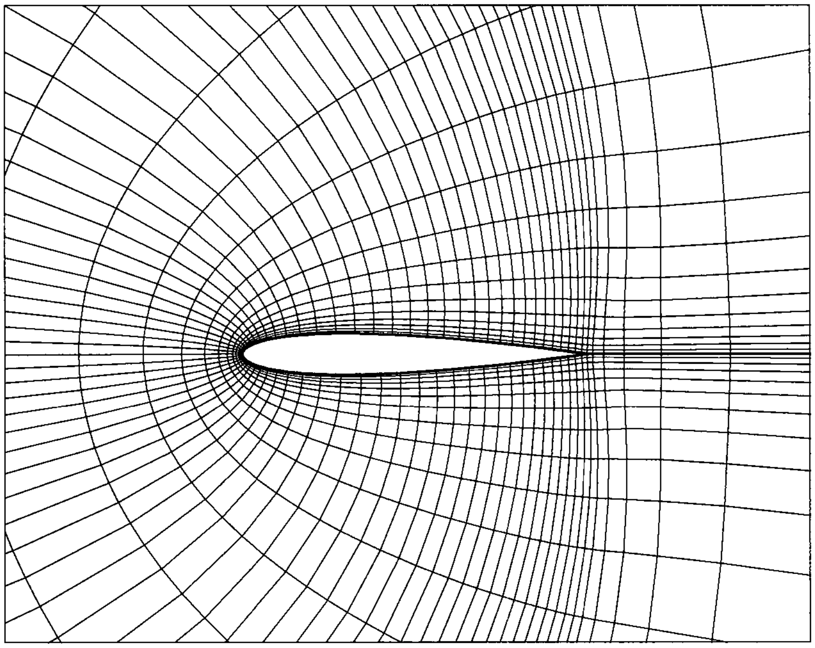

(a) Mesh 91×20

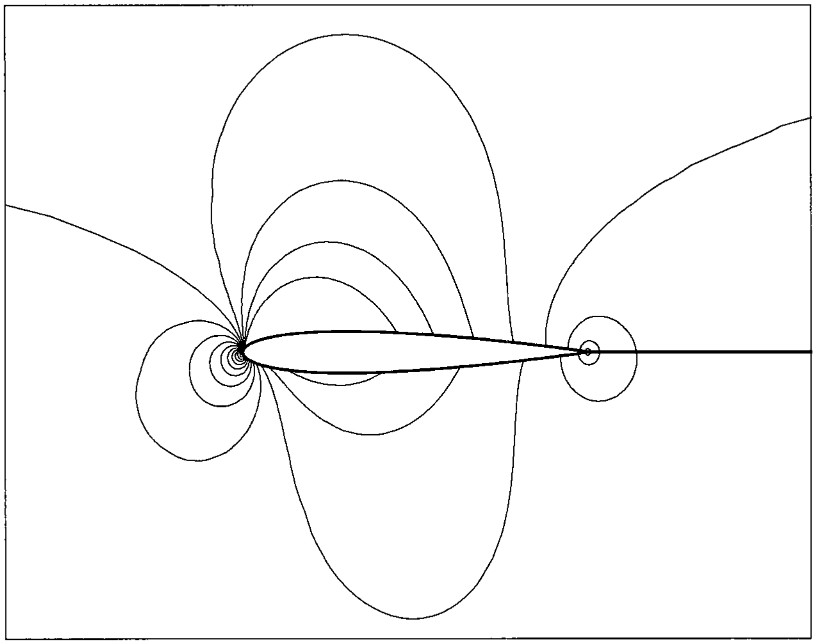

(b) c_p contours, 65520 D.o.f

Figure 4–7: NACA 0012, $M_\infty = 0.5$, $\alpha = 2^o$: Third-order computation

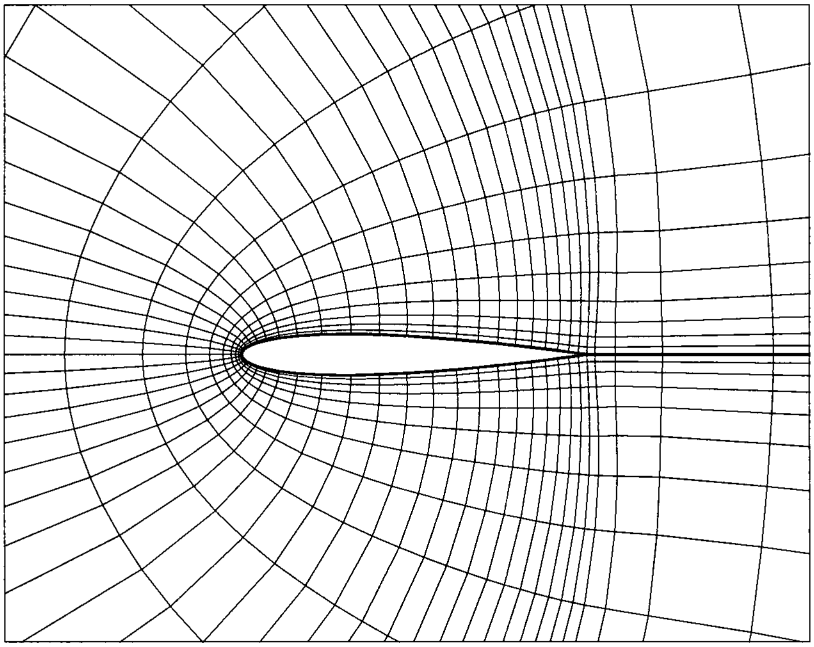

(a) Mesh 64×16

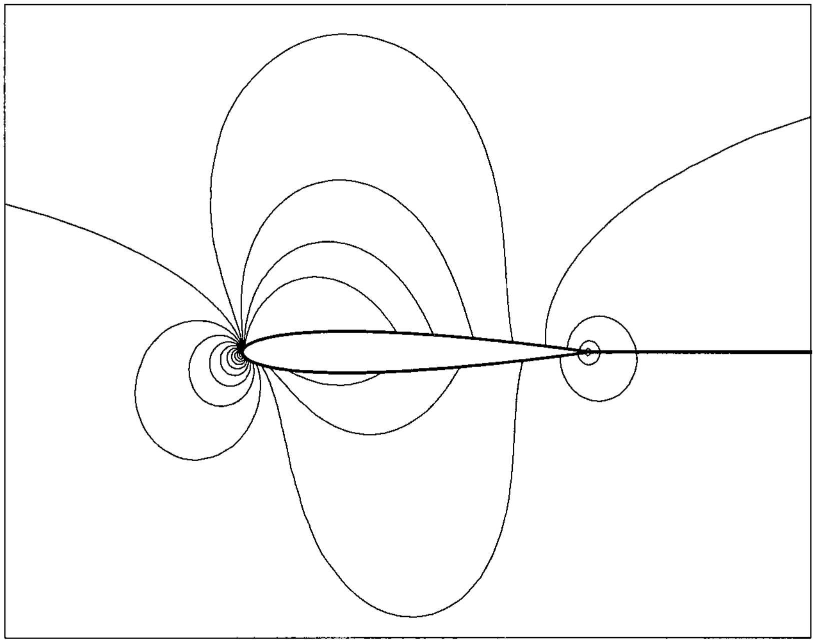

(b) c_p contours, 65536 D.o.f

Figure 4–8: NACA 0012, $M_\infty = 0.5$, $\alpha = 2^o$: Fourth-order computation

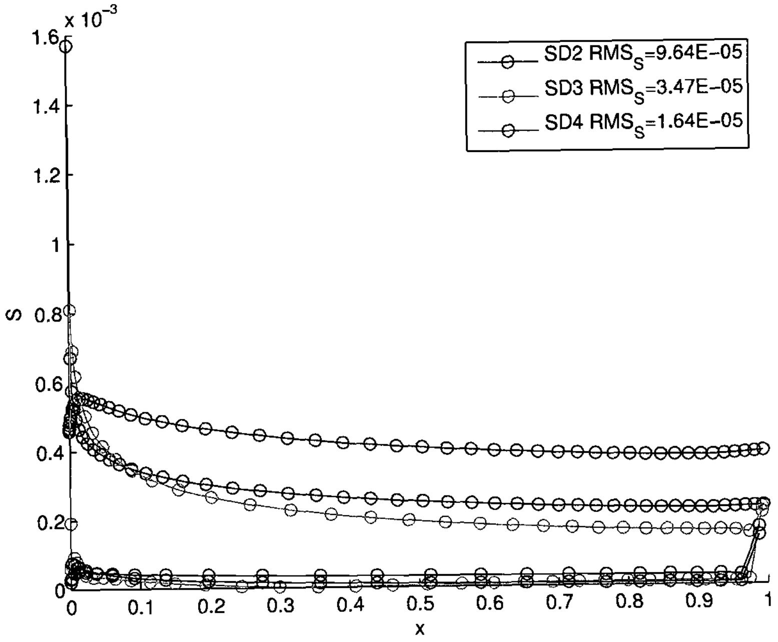

Figure 4–9: NACA 0012, $M_\infty = 0.5$, $\alpha = 2^o$: Entropy profile

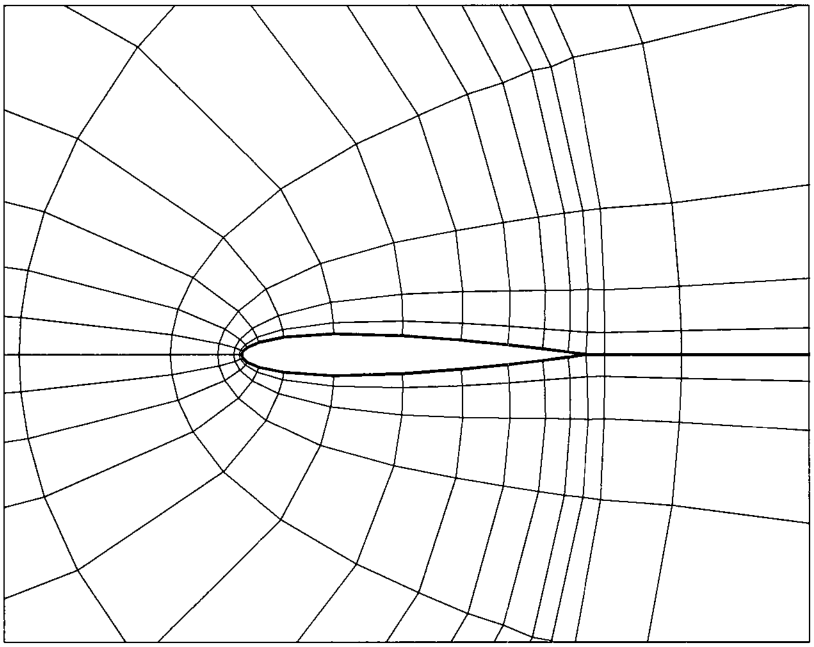

(a) Computational grid

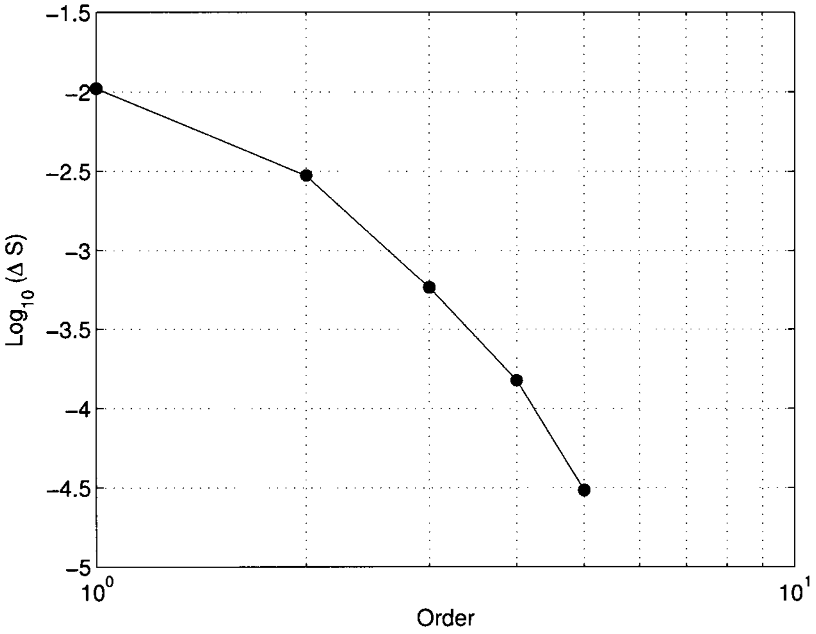

(b) Error v.s. order

Figure 4–10: NACA 0012, $M_\infty = 0.5$, $\alpha = 2^o$: Spectral convergence

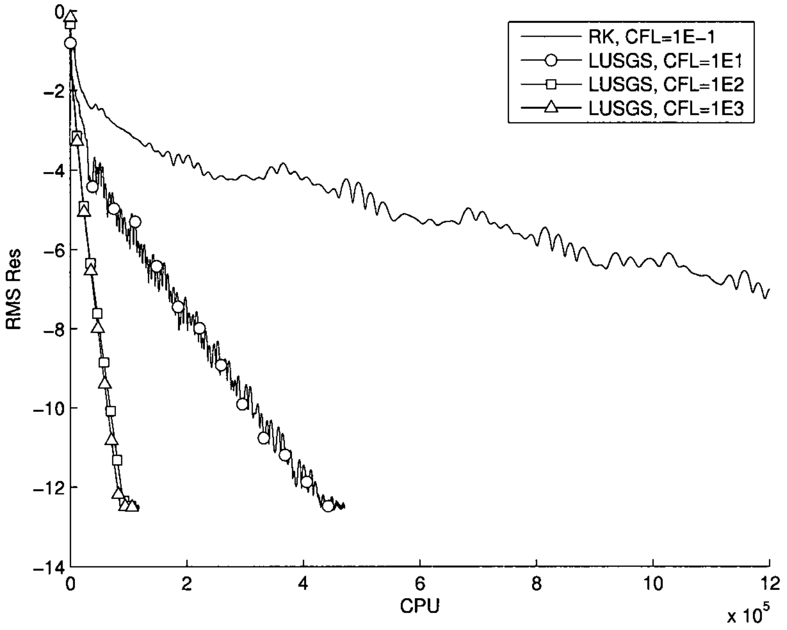

(a) Effect of time step

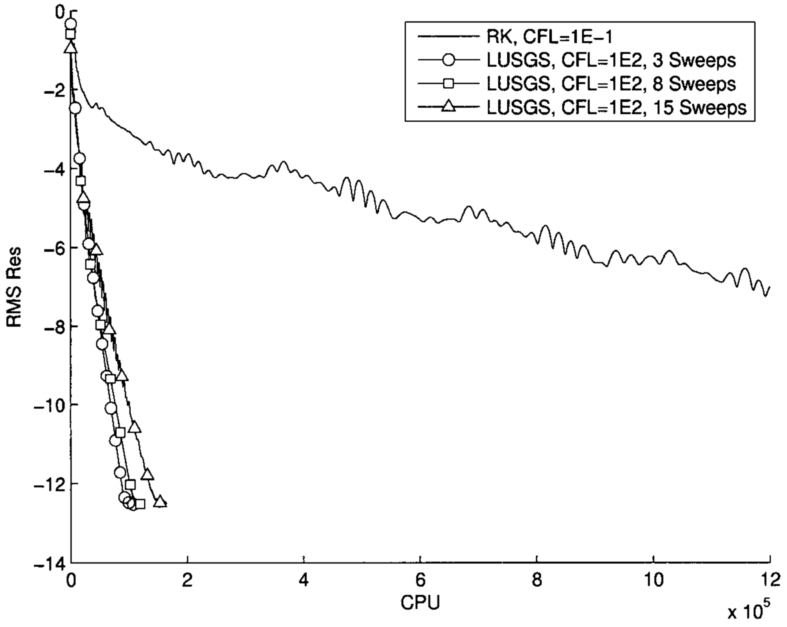

(b) Effect of number of sweeps

Figure 4-11: NACA 0012, $M_\infty = 0.5$, $\alpha = 2^o$: Comparison between the RK and LU-SGS schemes

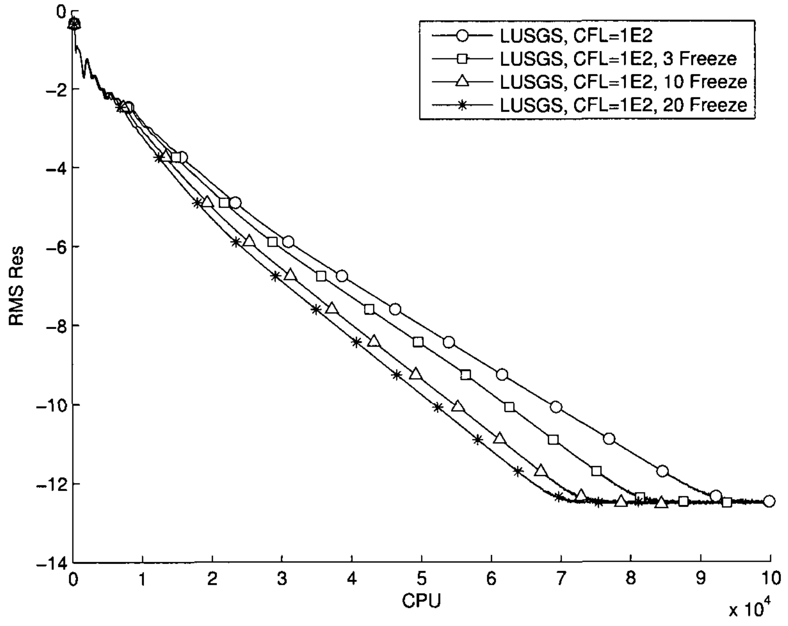

(a) Effect of freezing frequency

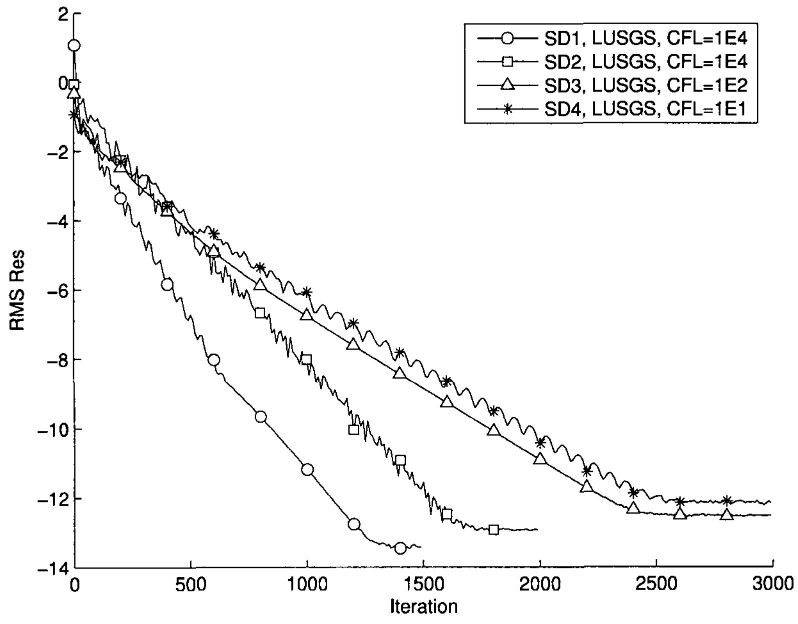

(b) Effect of scheme's order

Figure 4–12: NACA 0012, $M_\infty = 0.5$, $\alpha = 2^o$: Comparison between the RK and LU-SGS schemes contd.

4.3 Pitching Subsonic Airfoil

In this last validation problem, the full NLFD-SD scheme is employed to compute the the flow about an oscillating airfoil. This simulation problem serves as a demonstration for the proposed framework. The case examined consists of a pitching NACA64A010 airfoil at a free-stream Mach number of $M_\infty = 0.502$, the pitching movement being given by:

$$\alpha(t) = \alpha_m + \alpha_0 \cos(\omega t), \quad \text{about} \quad x/c = 0.269, \tag{4.7}$$

where $\alpha_m = -0.22^o$, $\alpha_o = 1.02^o$ with reduced frequency $\omega_r = \frac{\omega c}{2V_\infty} = 0.1$. This corresponds to the $CT = 2$ case of Davis [58], whose experimental results will be used to validate the scheme. Two examples of computational grids are shown in Fig. (4–13). We use a quadratic boundary representation, Rusanov's [50] numerical flux and three sweeps per time step for the LU-SGS solver.

Using the NLFD technique, we solve the flow for a given number of modes using the third-order spectral difference operator. First, the simulation is performed using a single mode above the fundamental frequency on a set of progressively finer grids ranging from 32×8 to 256×64. The spatial convergence of the lift coefficient for each time instance is presented in Table (4–2). It can be observed that using a 128×32 grid ($\approx 6 \times 10^5$ d.o.f) ensures that each lift coefficient is well within 1% of the final values. This resolution is then considered sufficiently fine for engineering precision and will be used for the subsequent computations.

Figure (4–14) presents the lift hysteresis obtained with 1, 2 and 3 modes above the fundamental frequency. As it can be noticed, the three curves are nearly indistinguishable, suggesting that a single mode is sufficient to capture the lift history. This is in agreement with McMullen[55] who also demonstrated the adequacy of a

Order	Grid	D.o.f.	c_l		
			$\alpha = -0.2200^o$	$\alpha = -1.1033^o$	$\alpha = 0.6633^o$
3	32×8	9216	-0.0137	-0.1278	0.0529
3	64×16	36864	-0.0130	-0.1312	0.0526
3	128×32	147456	-0.0124	-0.1323	0.0525
3	256×64	589824	-0.0124	-0.1323	0.0528
4	96×24	147456	-0.0126	-0.1324	0.0529

Table 4–2: NACA 64A010, $M_\infty = 0.502$, $\alpha_o = \pm 2^o$, $\omega_r = 0.1$: Lift convergence study

single mode for smooth inviscid flow around a pitching airfoil. To further confirm the convergence of the NLFD method, the real and imaginary parts of the first mode of c_p are plotted to monitor the unsteady pressure distribution in spectral space. Figure (4–15) shows that the three simulations yield similar results that are in excellent agreement with Davis' experimental values. The detail frame in Fig. (4–15b) confirms that one mode captures the general pressure trend. The curves representing the two and three modes simulations are completely overlapping, proving that mode-independence is achieved and that at least two modes are required to get converged pressure distributions.

To characterize the efficiency of the implicit NLFD-SD solver, the simulation using one mode is solved using the explicit five-stage RK method as well as the LU-SGS scheme using different parameters. Figure (4–16a) presents the comparison between the convergence rate obtained with each integration technique. As for the steady case, the LU-SGS allows for a larger time step and thus converges about twenty times faster. However, the detail frame shows that if the time step chosen is too large, the scheme becomes unstable and the first mode diverges, which may be attributed in part to the explicit treatment of the unsteady source term in equation (3.39) of the LU-SGS scheme. Nevertheless, a significant speedup is achieved, and this restriction is deemed acceptable. Further improvements are realized trough matrix freezing. Since each spectral Jacobian assembled requires to calculate multiple real space Jacobians, the gains realized are higher than that for the steady case. Figure (4–16b) shows that those Jacobians can indeed be frozen without loss of stability or efficiency. By keeping the same matrices for ten consecutive time steps, we see another 40% decrease in the computing time, making the scheme almost 30 times faster than the explicit solution. Figure (4–17) presents the comparison between the RK5 and LU-SGS with optimal parameters for simulations using two and three modes. As for the single mode case, the LU-SGS strategy has a rate of convergence larger by more than an order of magnitude. It is also shown that all modes converge approximately at the same rate for both the explicit and implicit solvers. Lastly, we compare the convergence rate of the fundamental frequency as shown in Fig. (4–18) and study the effect of increasing the number of modes. As illustrated, the convergence rates are almost identical with a slightly lower rate for the single mode case. Similar results can be obtained using the fourth-order spectral difference scheme together with the NLFD. Table (4–2) shows that even on a coarse grid, the predicted c_l values are in agreement with the fine (256×64), third-order simulations. A convergence plot for that simulation is presented on Fig. (4–19).

Next, the NLFD method is compared and numerically validated against a time accurate strategy. With that intent, we repeat the case of Davis using the dual time stepping scheme (DTS) presented in subsection (3.2.3). To allow a fair comparison, both NLFD and DTS use the same spatial discretization. The computational mesh of size 38×8 is illustrated on Fig. (4–13 b) and is used together with a third-order SD formulation. Moreover, each time step of the DTS computation is solved to machine zero, as shown on Fig. (4–20). The obtained lift coefficient evolution using

1024 time steps per period is presented on Fig. (4–21) and compared to the NLFD results using 8 modes. A perfect qualitative agreement is obtained between the two solutions. Tables (4–3) and (4–4) present the mean and first modes of c_l as the temporal resolution is increased. It can be noticed that the final values agree to the fifth significant digit, implying that both schemes are mathematically equivalent at convergence. To reach this convergence criterion, the NLFD needed 7 modes and required a CPU time of $2e5$. To achieve the same periodic solution, the time accurate strategy needed 1024 time steps over 7 periods, and required a CPU time of $1.6e6$. On that basis, a speedup of eight is reported for that test case.

Modes	$\bar{c}_l$	$\hat{c}_l$
1	-.3006177e-01	.9622533e-02 + .5233166e-01i
2	-.3069420e-01	.9699423e-02 + .5235933e-01i
3	-.3065299e-01	.9860353e-02 + .5271320e-01i
4	-.3064547e-01	.9869166e-02 + .5268716e-01i
5	-.3067235e-01	.9872353e-02 + .5271095e-01i
6	-.3066414e-01	.9873912e-02 + .5271737e-01i
7	-.3066367e-01	.9873386e-02 + .5271651e-01i
8	-.3066368e-01	.9873379e-02 + .5271649e-01i

Table 4–3: NLFD, $\bar{c}_l$ and $\hat{c}_l$

Time steps	$\bar{c}_l$	$\hat{c}_l$
12	-.3055247e-01	.9117501e-02 + .5187977e-01i
24	-.3063185e-01	.9692436e-02 + .5239203e-01i
32	-.3065331e-01	.9778853e-02 + .5251898e-01i
48	-.3066665e-01	.9836489e-02 + .5262420e-01i
64	-.3066744e-01	.9865998e-02 + .5269342e-01i
128	-.3066621e-01	.9869606e-02 + .5270356e-01i
192	-.3066499e-01	.9871778e-02 + .5271083e-01i
256	-.3066446e-01	.9872511e-02 + .5271332e-01i
512	-.3066387e-01	.9873183e-02 + .5271570e-01i
1024	-.3066372e-01	.9873328e-03 + .5271630e-01i

Table 4–4: Dual time stepping, $\bar{c}_l$ and $\hat{c}_l$

As a final demonstration of the robustness of the NLFD-SD scheme, we perform the simulation on two additional reduced frequencies, $\omega_r = 0.05$ and $\omega_r = 0.2$. Figures (4–22) present the lift hysteresis for each of these runs. Once more, the curve representing one, two and three modes above the fundamental frequency overlap, indicating a mode-converged simulation. For reference, the lift hysteresis of the previous case is also presented. We observe that the increased reduced frequency induces the maximum lift produced in the flow cycle. Figures (4–23 illustrate the unsteady pressure distribution in spectral space. Both the real and imaginary pressure distributions confirm that one mode is sufficient; however, from the inset at least two are required to get a converged pressure distribution. CPU run times are presented in Fig. (4–24 a) and are very comparable with (4–17 b), illustrating the independence of the implicit solver with respect to the simulated flow condition. Lastly, Fig. (4–24 b) shows the convergence of the lift coefficient at several different time instances as a periodic steady state flow is realized. Clearly, the c_l values of each time instance stabilize well before the residual reaches machine zero, indicating that the periodic simulation can be halted prematurely if engineering accuracy is required.

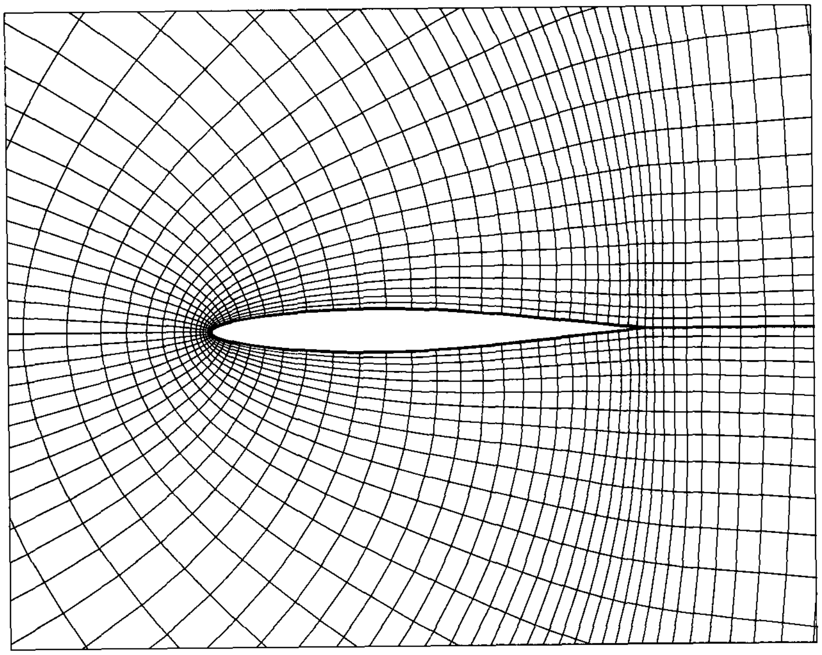

(a) 128×32

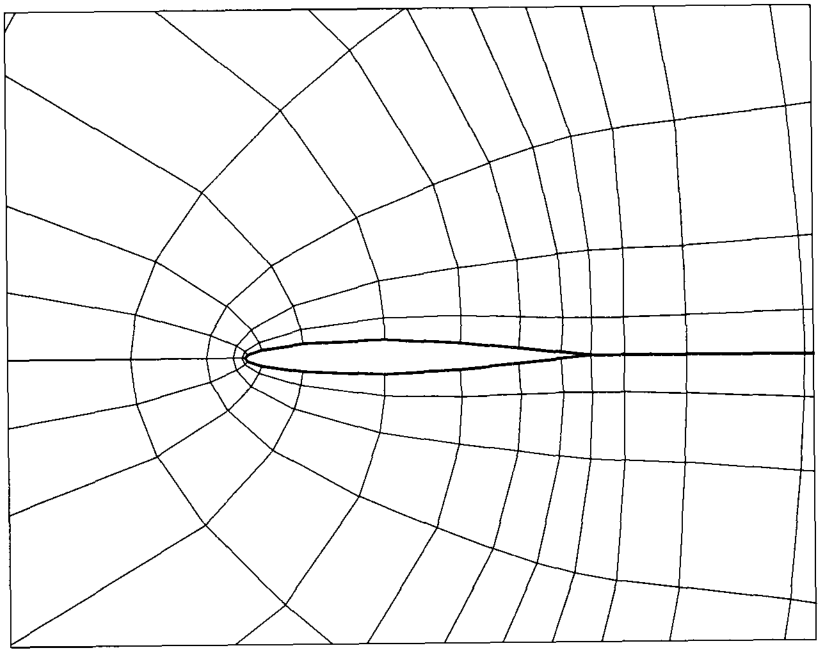

(b) 32×8

Figure 4–13: NACA 64A010: Computational meshes

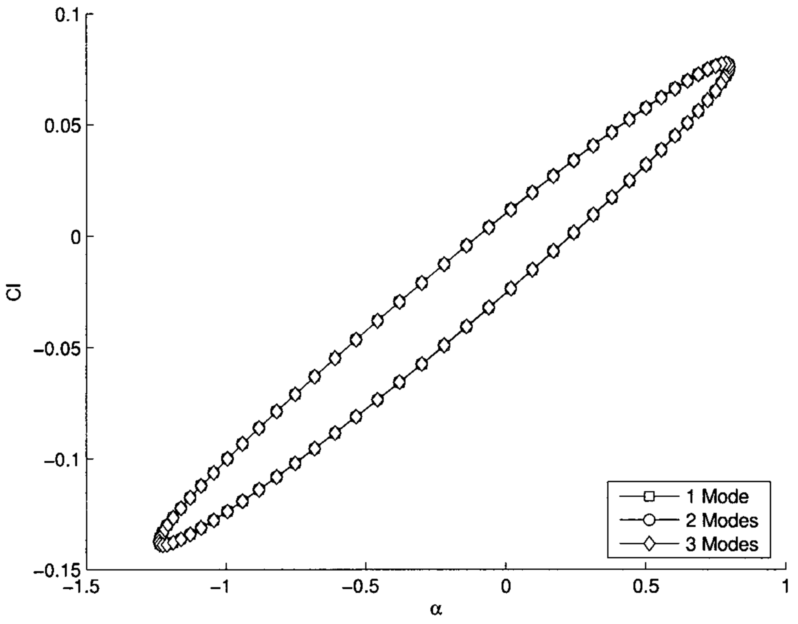

Figure 4–14: NACA 64A010, $M_\infty = 0.502$, $\alpha_o = \pm 2^o$, $\omega_r = 0.1$: c_l hysteresis

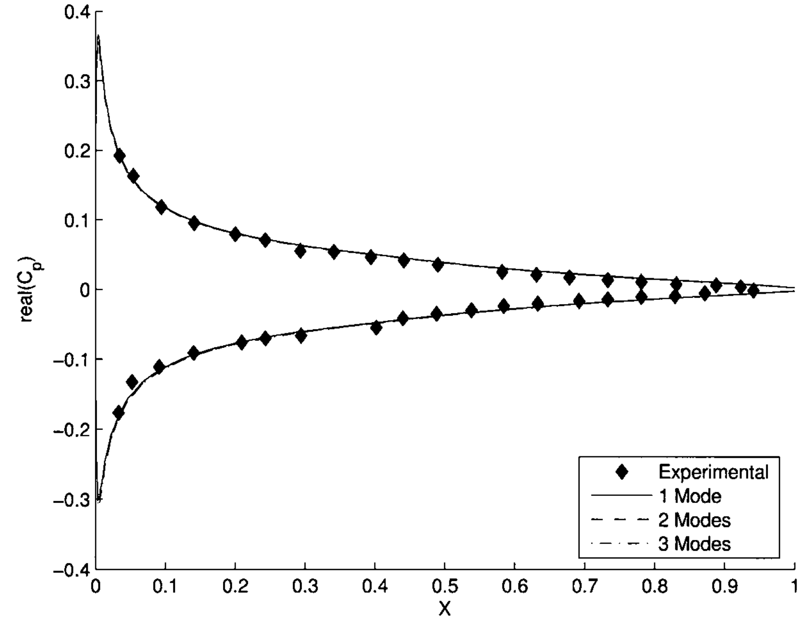

(a) real($\hat{c_p}$)

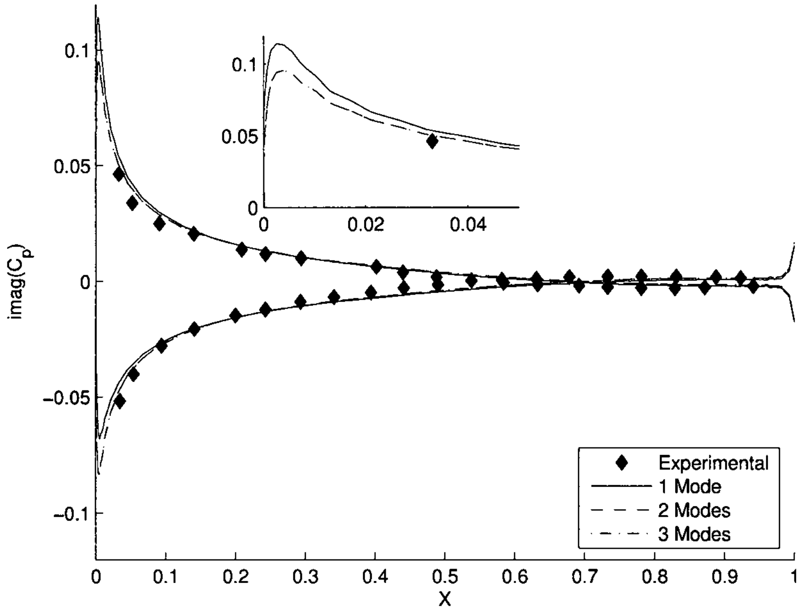

(b) imag($\hat{c_p}$)

Figure 4–15: Numerical and experimental first mode of c_p

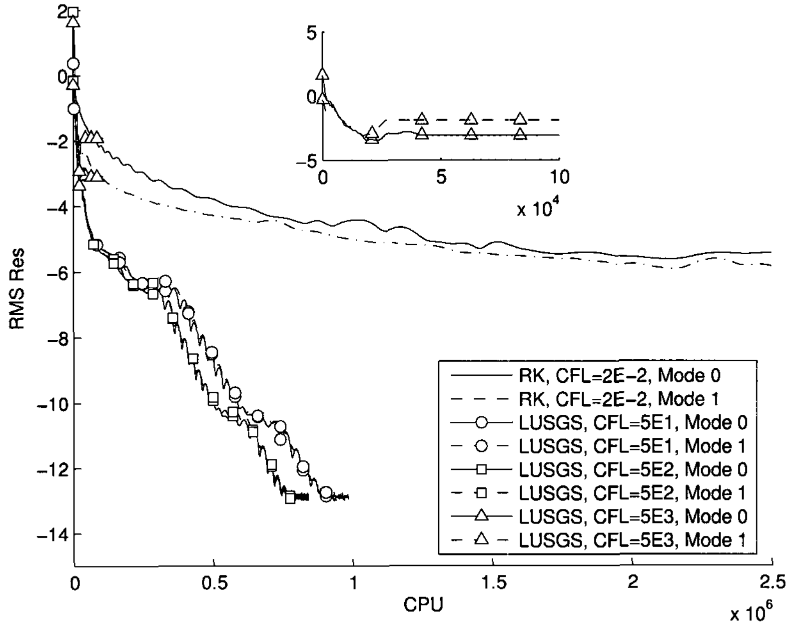

(a) Effect of time step

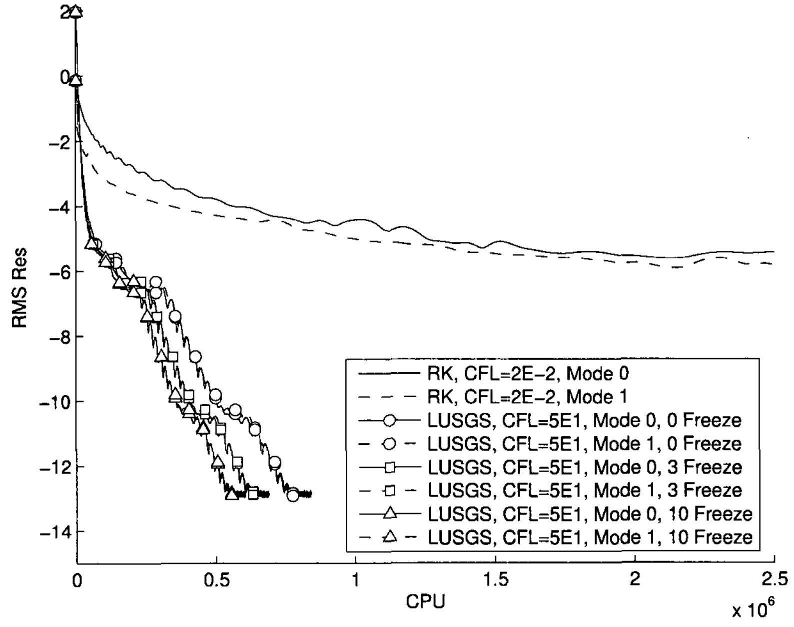

(b) Effect of matrix freezing

Figure 4–16: Comparison between the RK5 and LU-SGS schemes for a one-mode NLFD simulation

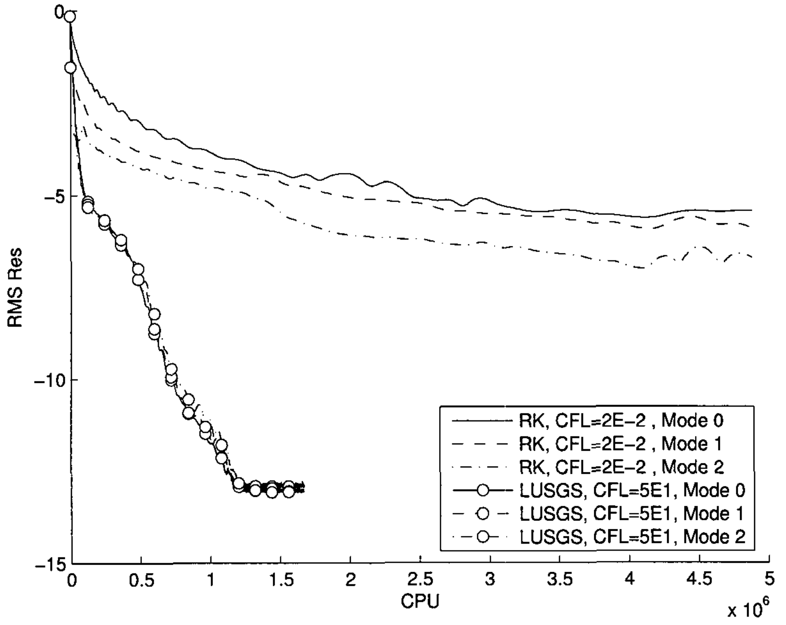

(a) 2 modes

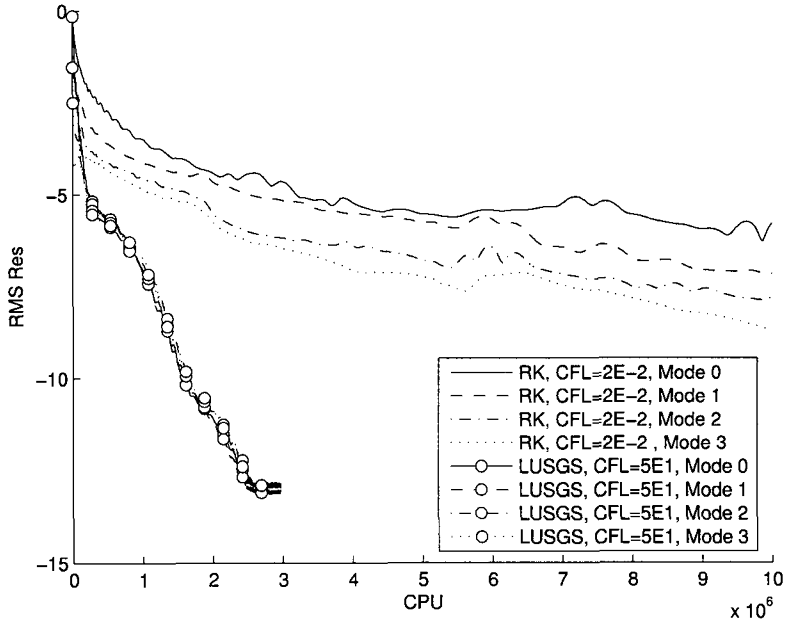

(b) 3 modes

Figure 4–17: Comparison between the RK5 and LU-SGS schemes for two and three modes NLFD simulations

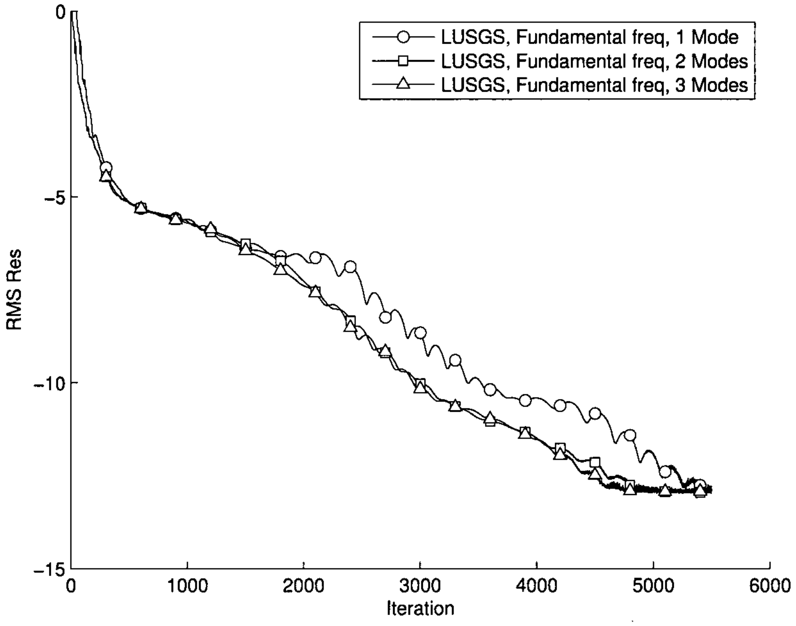

Figure 4–18: Effect of the number of modes on the convergence rate of the zeroth mode

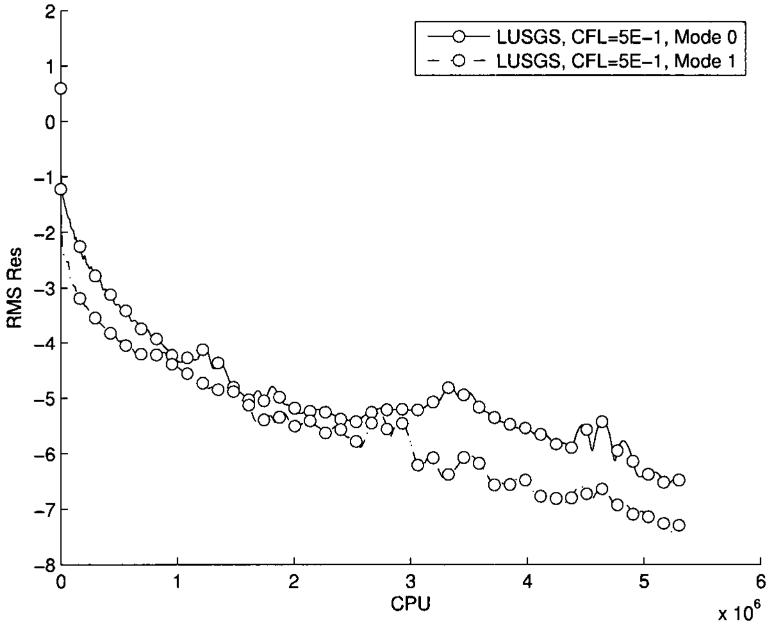

Figure 4–19: SD4, 96 × 24, 1 mode: Residual convergence

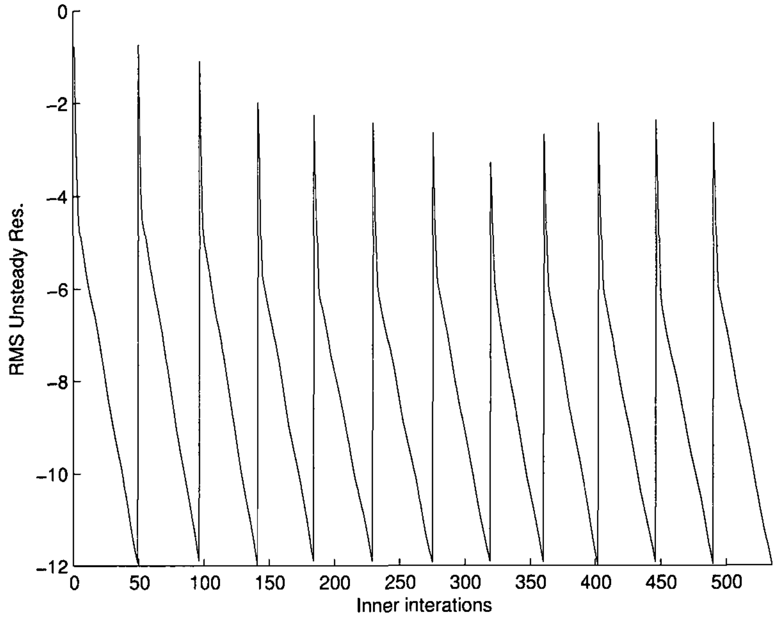

Figure 4–20: Dual time stepping (12 steps/period): Inner iterations convergence for the first period

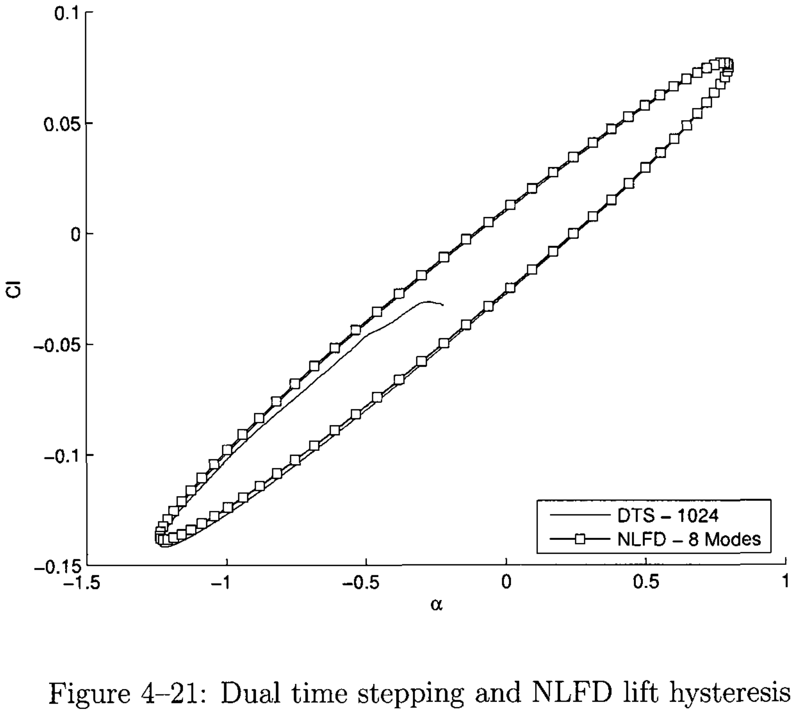

Figure 4–21: Dual time stepping and NLFD lift hysteresis

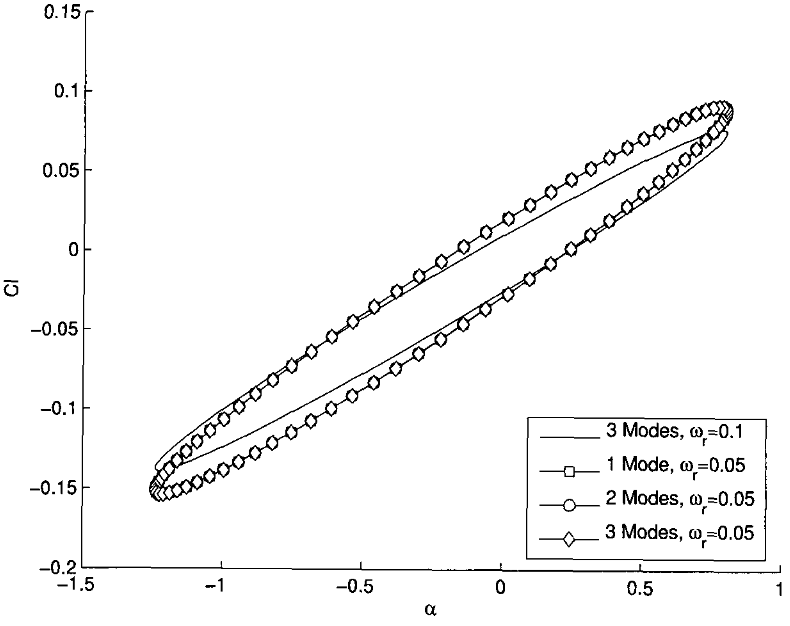

(a) $c_l(\alpha)$, $\omega_r = 0.05$

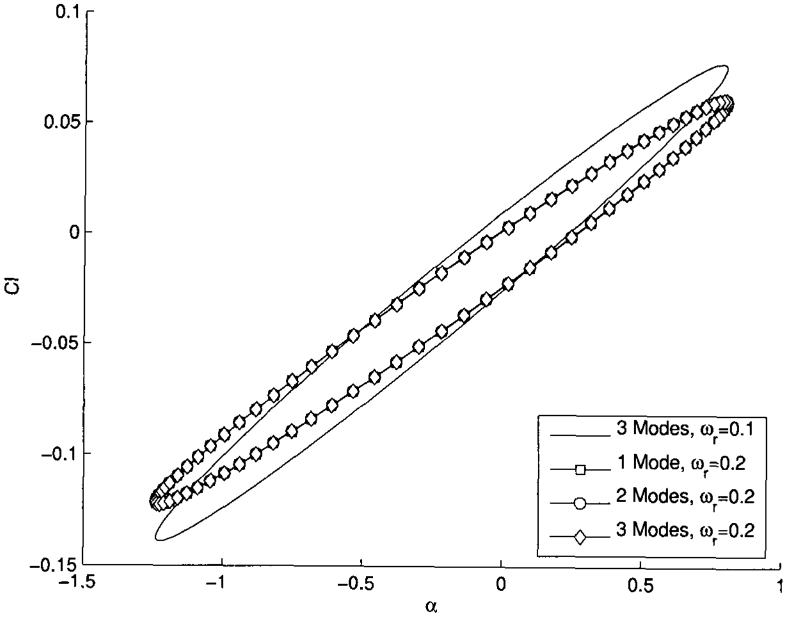

(b) $c_l(\alpha)$, $\omega_r = 0.2$

Figure 4–22: NACA64A010, $\omega_r = 0.05$ and $\omega_r = 0.2$: Lift hysteresis

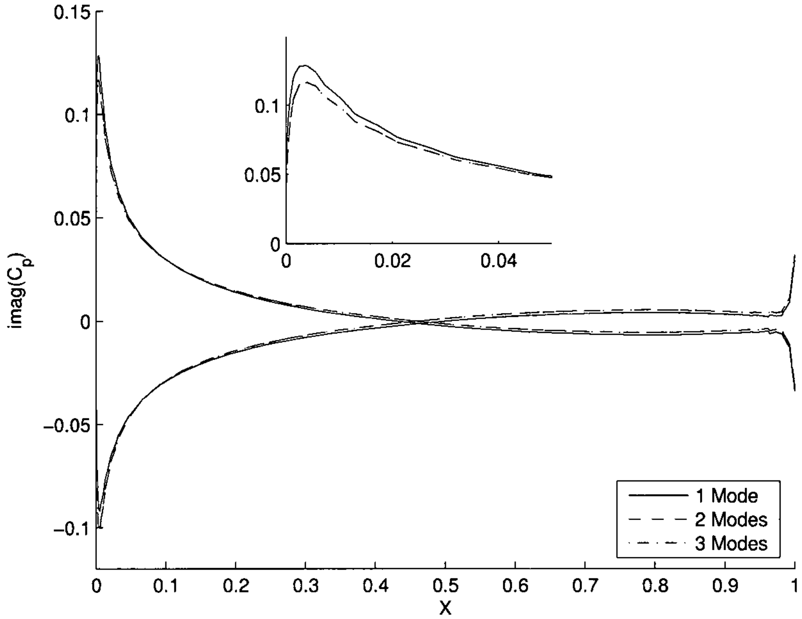

(a) imag($\hat{c_p}$), $\omega_r = 0.2$

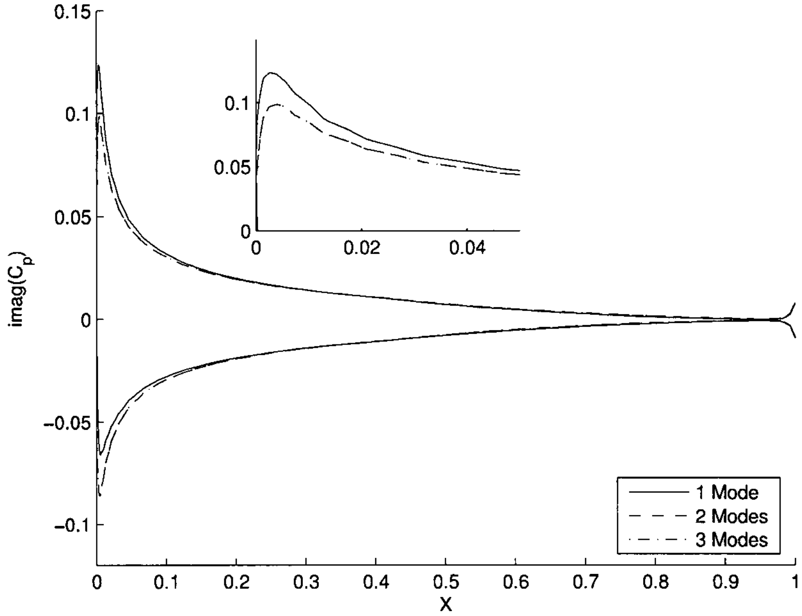

(b) imag($\hat{c_p}$), $\omega_r = 0.05$

Figure 4–23: NACA64A010, $\omega_r = 0.2$ and $\omega_r = 0.2$: Unsteady pressure distribution

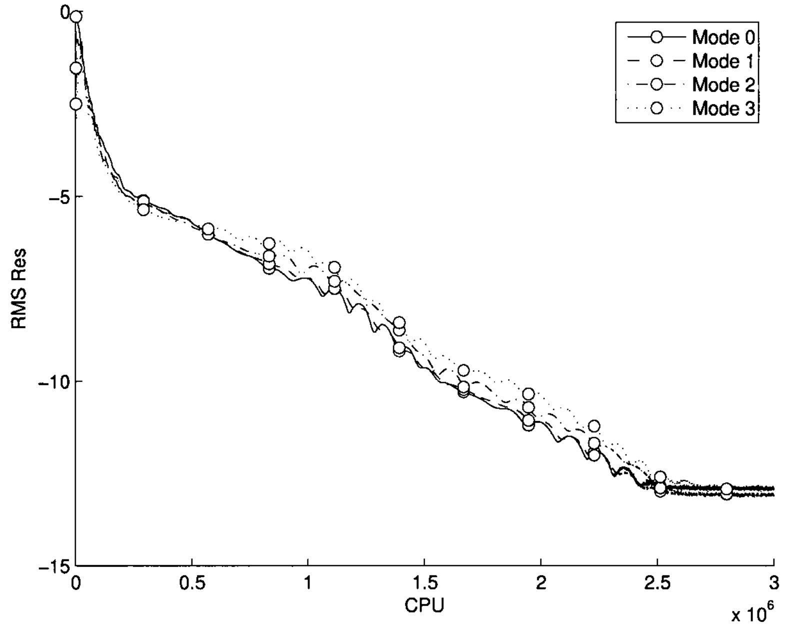

(a) Residual convergence, 3 modes, $\omega_r = 0.2$

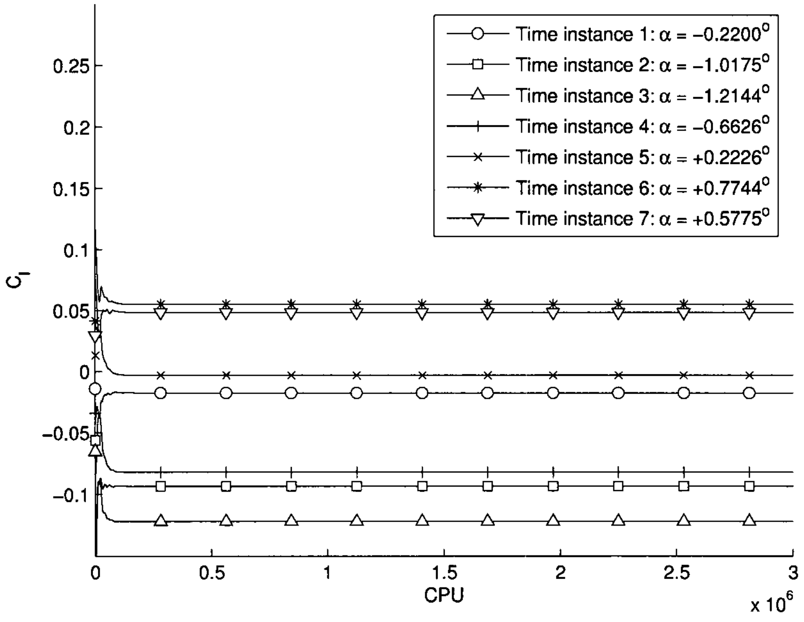

(b) c_l convergence, 3 modes, $\omega_r = 0.2$

Figure 4–24: NACA64A010, and $\omega_r = 0.2$: Residual and lift convergence

CHAPTER 5
Conclusion

An high-order scheme in both space and time has been developed to efficiently tackle the simulation of potentially complex, compressible flow phenomena with periodic solutions. This newly developed NLFD-SD scheme was obtained by combining a high-order spectral-difference space discretization with a non-linear frequency domain approach. For more efficiency, an implicit lower-upper symmetric Gauss-Seidel solver was introduced to solve the resulting set of non-linear equations. This chapter recapitulates the results demonstrated in this thesis, and opens the door to possible future work.

5.1 Space Discretization

The research presented focused on the high-order discretization of the Euler equations. A parametric study for the vortex advection problem and the steady subsonic NACA0012 airfoil was realized. From these cases, it was demonstrated that high-order solutions are consistently more accurate than lower-order ones, even for an equal number of unknowns. Moreover, we showed that spectral-like convergence may be obtained by refining the degree of the polynomial flow representation. The accuracy and flexibility offered by this approach will be key in tackling complex, vortex-dominated problems for which this scheme is designed.

5.2 Temporal discretization

The implemented spectral-difference solver was tested with various temporal discretization. Firstly, a multistage Runge-Kutta scheme and an implicit LU-SGS were compared. We showed that when calibrated optimally, the LU-SGS converged to steady state as much as 30 times faster and its explicit counterpart, while preserving the high-order accuracy of the space discretization. In a second time, the SD solver was augmented with the NLFD spectral temporal discretization, and we demonstrated the feasibly of the NLFD-SD scheme on a pitching airfoil simulation. On this test case, we obtained an excellent agreement with the available wind tunnel data, and showed that only two temporal modes are required to capture the full unsteadiness of the flow. More over, we also adapted the LU-SGS scheme for the solution of the NLFD equations. Numerical experiment demonstrated that the novel implicit approach accelerated the convergence by over an order of magnitude. Finally the framework was thoroughly validated against the dual time stepping approach. The mathematical equivalence of both approaches was proven numerically, and the NLFD scheme presented a speed-up factor of eight over the time accurate scheme.

5.3 Future Work

The results presented in this thesis provide a strong foundation for future work. Some potential projects are listed below.

5.3.1 Strong Non-Linearities

One obvious extension of the work presented in this thesis is the application of the scheme to strongly non-linear unsteady flows. This would imply extending the solver to the transonic regime and including viscous effects in the formulation. We have examined multiple alternatives to develop an effective and robust shock-capturing methodology for the spectral difference method. Although optimal limiting strategies for the DG, SV and SD scheme is still an open topic, our current developments are showing encouraging results. Figure (5–1) shows a second-order steady transonic computation. In the vicinity of the shock, a shock detector is employed to trigger flux limiting within the SD scheme. This approach stabilizes the scheme near steep gradients while retaining a sharp shock profile. Improved monotonicity criterion and overall robustness are currently explored.

5.3.2 Adaptive Solution Method

Another interesting avenue to investigate would be the incorporation of an adaptive solution methodology in the NLFD-SD solver. Firstly, the performance and accuracy of the method could easily be increased by allowing a variation of the solution polynomial from cell to cell. Secondly, the mesh could be optimized as the solution progresses. Thirdly, the number of modes utilized could be adjusted to the strength of the local unsteadiness.

Figure (5–2) presents preliminary p-adaptation results for a steady subsonic NACA airfoil. The case is computed with the second-order and third-order SD, as well as a mixed formulation. For the latter case, the cells near the airfoil were manually flagged to employ a third-order polynomial, while the rest of the domain uses the cheaper second-order formulation, as shown of Fig. (5–3). For the mesh resolution chosen, the second-order scheme is clearly inadequate and only the third-order scheme produces an acceptable solution. The mixed formulation however, achieves similar results as the third-order scheme at a fraction of the computational cost, as it can be verified on Fig. (5–4). Table (5–1) where the lift, drag and entropy values are presented confirms this trend. Coupled with an error estimation algorithm, this adaptive solution method could be a reliable and efficient path to high-quality solutions, in a fully automated manner.

	c_l	c_d	Entropy
2^{nd} order	0.65787	0.00225	5.640e-04
3^{rd} order	0.66785	0.00039	7.038e-05
Mixed	0.66322	0.00087	6.852e-05

Table 5–1: NACA 0012, $M_\infty = 0.4$, $\alpha = 5^o$: Force coefficients and spurious entropy level

5.3.3 Alternative SD formulations

The NLFD-SD scheme is largely independent of the type of SD scheme employed. Consequently, other location of the solution and flux points could be employed, perhaps leading to improved numerical properties. An extension the unstructured and three-dimensional grids would also be of interest.

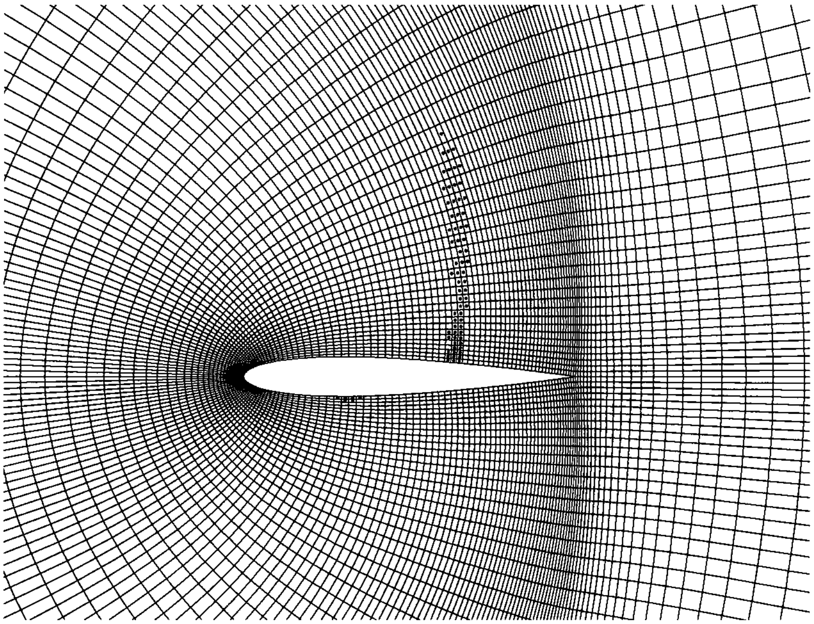

(a) Mesh 256×64: Limited cells

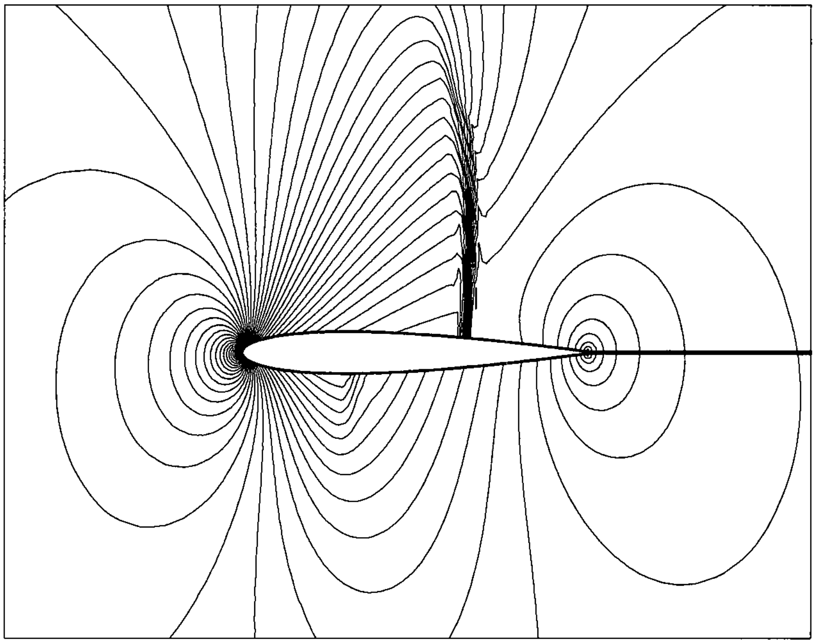

(b) c_p contours

Figure 5–1: NACA 0012, $M_\infty = 0.8$, $\alpha = 1.25^o$: Second-order computation

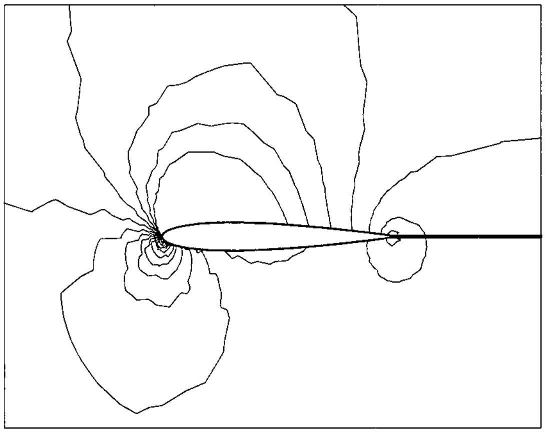

(a) Second-order

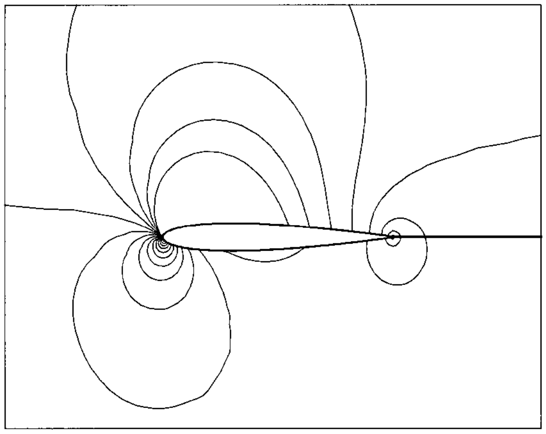

(b) Third-order

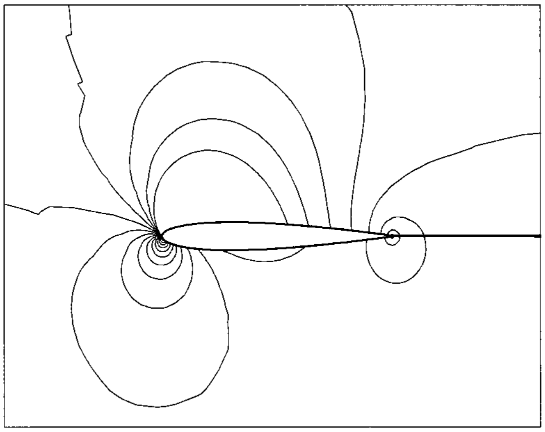

(c) Mixed

Figure 5–2: NACA 0012, $M_\infty = 0.4$, $\alpha = 5^o$: Second-order, third-order, Mixed

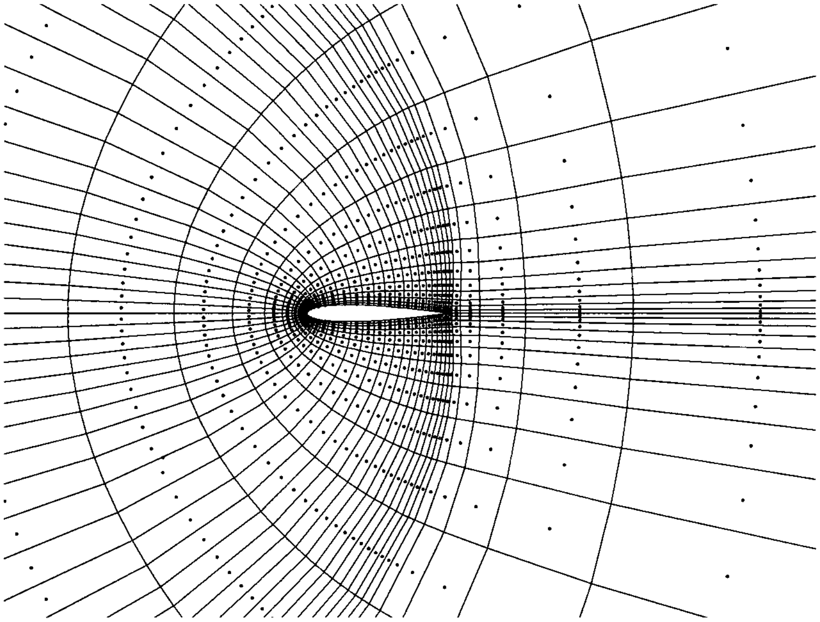

Figure 5–3: NACA 0012, $M_\infty = 0.4$, $\alpha = 5^o$: Second-Order (•), Third-order (•)

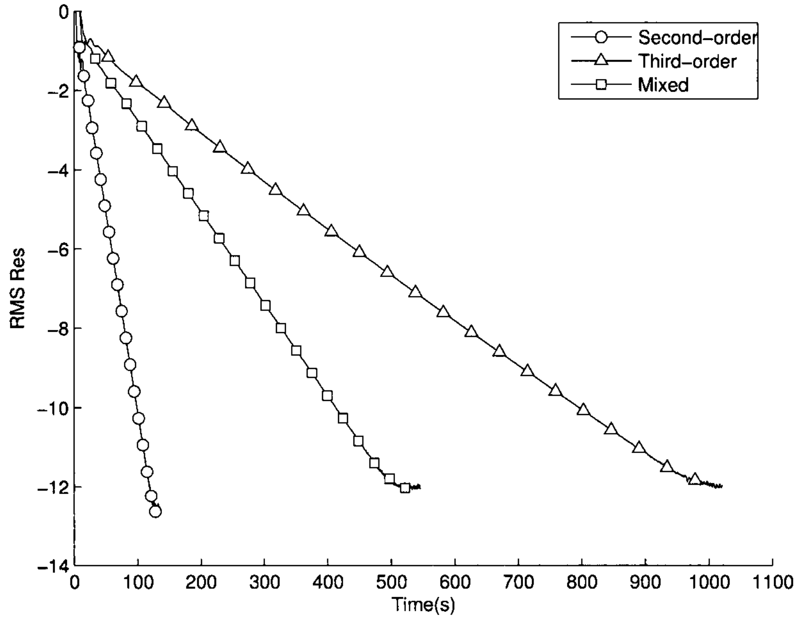

Figure 5–4: NACA 0012, $M_\infty = 0.4$, $\alpha = 5^o$: Convergence

Appendix A

For the computation of the metric terms, two possibility arise as domain cells have straight edges, while cells near solid wall have curved edges. For both cases, we can write the transformation from computational to physical space using the inverse metrics

$$\begin{bmatrix} x \\ y \end{bmatrix} = \begin{bmatrix} x_\xi & x_\eta \\ y_\xi & y_\eta \end{bmatrix} \begin{bmatrix} \xi \\ \eta \end{bmatrix} .$$

Consequently, the direct metrics terms are obtained by inverting the system

$$\begin{aligned} \xi_x &= \frac{1}{J}\, y_\eta, \\ \xi_y &= -\frac{1}{J}\, x_\eta, \\ \eta_x &= -\frac{1}{J}\, y_\xi, \\ \eta_y &= \frac{1}{J}\, x_\eta, \\ J &= x_\xi\, y_\eta - x_\eta\, y_\xi. \end{aligned}$$

In the case of domain cells, the cell geometry is defined by its four vertex, as shown on Fig. (5–5).

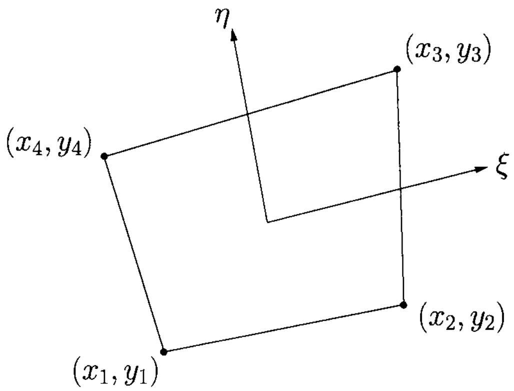

Figure 5–5: Definition of a straight-sided cell

The direct metric terms are given by

$$\begin{aligned}
x_\xi &= \frac{1}{4}\left(-x_1+x_2+x_3-x_4\right)+\frac{\eta}{4}\left(x_1-x_2+x_3-x_4\right),\\
x_\eta &= \frac{1}{4}\left(-y_1+y_2+y_3-y_4\right)+\frac{\eta}{4}\left(y_1-y_2+y_3-y_4\right),\\
y_\xi &= \frac{1}{4}\left(-x_1-x_2+x_3+x_4\right)+\frac{\xi}{4}\left(x_1-x_2+x_3-x_4\right),\\
y_\eta &= \frac{1}{4}\left(-y_1-y_2+y_3+y_4\right)+\frac{\xi}{4}\left(y_1-y_2+y_3-y_4\right).
\end{aligned}$$

In the case of boundary cells, a mid-edge node is added to the four vertex to accommodate curved walls.

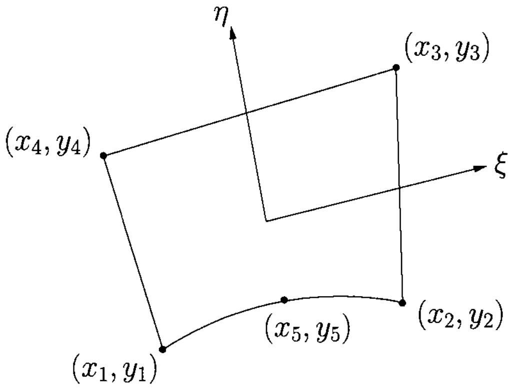

Figure 5–6: Definition of a boundary cell

The direct metric terms are given by

$$\begin{aligned}
x_\xi &= \frac{1}{4}\left(-x_1+x_2+x_3-x_4\right)+\frac{\xi}{2}\left(x_1+x_2-2x_5\right)\\
&+ \frac{\eta}{4}\left(x_1-x_2+x_3-x_4\right)+\frac{\xi\eta}{2}\left(-x_1-x_2+2x_5\right)\\
x_\eta &= \frac{1}{4}\left(-y_1+y_2+y_3-y_4\right)+\frac{\xi}{2}\left(y_1+y_2-2y_5\right)\\
&+ \frac{\eta}{4}\left(y_1-y_2+y_3-y_4\right)+\frac{\xi\eta}{2}\left(-y_1-y_2+2y_5\right)\\
y_\xi &= \frac{1}{4}\left(x_3+x_4-2x_5\right)+\frac{\xi}{4}\left(x_1-x_2+x_3-x_4\right)+\frac{\xi^2}{4}\left(-x_1-x_2+2x_5\right)\\
y_\eta &= \frac{1}{4}\left(y_3+y_4-2y_5\right)+\frac{\xi}{4}\left(y_1-y_2+y_3-y_4\right)+\frac{\xi^2}{4}\left(-y_1-y_2+2y_5\right)
\end{aligned}$$

References

[1] S.K. Godunov. A finite-difference method for the numerical computation of discontinuous solutions of the equations of fluid dynamics. *Mat. Sb.*, 47:47–271, 1959.

[2] B. Van Leer. Towards the ultimate conservative difference scheme II: Monotonicity and conservation combined in a second-order scheme. *Journal of Computational Physics*, 14:361–370, 1974.

[3] B. Van Leer. Towards the ultimate conservative difference scheme V: A second order sequel to Godunov's method. *Journal of Computational Physics*, 32:101–136, 1979.

[4] P. Collela and P. Woodward. The piecewise parabolic method for gas-dynamical simulations. *Journal of Computational Physics*, 54:174–201, 1984.

[5] J.A. Ekaterinaris. High-order accurate, low numerical diffusion methods for aerodynamics. *Progress in Aerospace Sciences*, 41:192–300, 2005.

[6] Z.J. Wang. High-order methods for the Euler and Navier-Stokes equations on unstructured grids. *Progress in Aerospace Sciences*, 43:1–41, 2007.

[7] A. Harten, B. Enquist, S. Osher, and S. Chakravarthy. Uniformly high-order essentially non-oscillatory schemes III. *Journal of Computational Physics*, 71:231–303, 1987.

[8] A. Harten and S. Osher. Uniformly high-order essentially non-oscillatory schemes I. *SIAM Journal of Numerical Analysis*, 24:279–309, 1987.

[9] A. Harten and S. Chakravarthy. Multi-dimensional ENO schemes for general geometries. ICASE Report No. 91- 76, 1991.

[10] R. Abgrall. On essentially non-oscillatory schemes on unstructured meshes: Analysis and implementation. *Journal of Computational Physics*, 114:4558, 1994.

[11] L.J. Durlofsky, B. Enquist, and S. Osher. Triangle based adaptive stencils for the solution of hyperbolic conservation laws. *Journal of Computational Physics*, 1:92–73, 1992.

[12] C.F. Ollivier-Gooch. Quasi-ENO schemes for unstructured meshes based on unlimited data-dependent least-squares reconstruction. *Journal of Computational Physics*, 133:6–17, 1997.

[13] T. Sonar. On the construction of essentially non-oscillatory finite volume approximations to hyperbolic conservation laws on general triangulations: Polynomial recovery accuracy and stencil selection. *Computer Methods in Applied Mechanics and Engineering*, 140:157–81, 1997.

[14] G.S. Jiang and C.W. Shu. Efficient implementation of weighted ENO schemes. *Journal of Computational Physics*, 1:202–228, 1996.

[15] X.D. Liu, S. Osher, and T. Chan. Weighted essentially non-oscillatory schemes. *Journal of Computational Physics*, 150:561–594, 1999.

[16] O. Friedrich. Weighted essentially non-oscillatory schemes for the interpolation of mean values on unstructured grids. *Journal of Computational Physics*, 144:194–212, 1998.

[17] C. Hu and C.W. Shu. Weighted essentially non-oscillatory schemes on triangular meshes. *Journal of Computational Physics*, 150:97–127, 1999.

[18] C.-W. Shu. *Essentially Non-Oscillatory and Weighted Essentially Non-Oscillatory Schemes for Hyperbolic Conservation Laws*, volume 1697, page 325. Springer-Verlag, Berlin/New York, lecture notes in mathematics edition, 1998.

[19] W.H. Reed and T.R. Hill. Triangular mesh methods for the neutron transport equation. Technical Report LA-UR-73479, Los Alamos Scientific Laboratory, 1973.

[20] B. Cockburn and C.W. Shu. TVB Runge-Kutta local projection discontinuous Galerkin finite element method for conservation laws II: General framework. *Mathematic of Computation*, 52:411–435, 1989.

[21] B. Cockburn and C.W. Shu. The Runge-Kutta discontinuous Galerkin method for conservation law III: One-dimensional systems. *Journal of Computational Physics*, 84:90–113, 1989.

[22] B. Cockburn, S. Hou, and C.W. Shu. The Runge-Kutta discontinuous Galerkin method for conservation law IV: The multidimensional case. *Mathematic of Computation*, 54:545–581, 1990.

[23] B. Cockburn and C.W. Shu. The Runge-Kutta discontinuous Galerkin method for conservation law V: Multidimensional systems. *Journal of Computational Physics*, 141:199–224, 1998.

[24] F. Bassi and S. Rebay. High-order accurate discontinuous finite element solution of the 2D Euler equations. *Journal of Computational Physics*, 138:251–285, 1997.

[25] F. Bassi and S. Rebay. A high-order accurate discontinuous finite element method for the numerical solution of the compressible Navier-Stokes equations. *Journal of Computational Physics*, 131:267–279, 1997.

[26] B. Cockburn and G.E. Karniadakis C.W. Shu. The development of discontinuous Galerkin methods. In *Discontinuous Galerkin methods.* B. Cockburn G.E. Karniadakis and C.W. Shu, editors. Springer, 2000.

[27] B. Cockburn and C.W. Shu. Runge-Kutta discontinuous Galerkin methods for convection-dominated problems. *Journal of Scientific Computing*, 16:173–261, 2001.

[28] Z.J. Wang. Spectral (finite) volume method for conservation laws on unstructured grids I: Basic formulation. *Journal of Computational Physics*, 178:210–251, 2002.

[29] Z.J. Wang and Y. Liu. Spectral (finite) volume method for conservation laws on unstructured grids II: Extension to two-dimensional scalar equation. *Journal of Computational Physics*, 179:665–697, 2002.

[30] Z.J. Wang and Y. Liu. Spectral (finite) volume method for conservation laws on unstructured grids III : One-dimensional systems and partition optimization. *Journal of Scientific Computing*, 20:137–157, 2004.

[31] Z.J. Wang, L. Zhang, and Y. Liu. Spectral (finite) volume method for conservation laws on unstructured grids IV: Extension to two-dimensional systems. *Journal of Computational Physics*, 194:716–741, 2004.

[32] Y. Liu, M. Vinokur, and Z.J. Wang. Spectral (finite) volume method for conservation laws on unstructured grids V: Extention to three-dimensional systems. *Journal of Computational Physics*, 212:454–472, 2006.

[33] Y. Sun, Z.J. Wang, and Y. Liu. Spectral (finite) volume method for conservation laws on unstructured grids VI: Extension to viscous flow. *Journal of Computational Physics*, 215:41–58, 2006.

[34] R. Harris, Z.J. Wang, and Y. Liu. Efficient quadrature-free high-order spectral volume method on unstructured grids: Theory and 2d implementation. *Journal of Computational Physics*, 227:16201642, 2008.

[35] D.A. Kopriva and J.H. Kolias. A conservative staggered-grid chebyshev multidomain method for compressible flows. *Journal of Computational Physics*, 125:244–261, 1996.

[36] D.A. Kopriva. A conservative staggered-grid chebyshev multidomain method for compressible flow II: A semi-structured method. *Journal of Computational Physics*, 128:475–488, 1996.

[37] Y. Liu, M. Vinokur, and Z.J. Wang. Spectral difference method for unstructured grids i: Basic formulation. *Journal of Computational Physics*, 216:780–801, 2006.

[38] Z.J. Wang and Y. Liu. The spectral difference method for the 2D Euler equations on unstructured grids. In *17th AIAA Computational Fluid Dynamics Conference*, Orlando, Florida, 2005. AIAA Paper 2005-5112.

[39] G. May and A. Jameson. A spectral difference method for the Euler and Navier-Stokes equations on unstructured meshes. In *44th. Aerospace Sciences Meeting and Exhibit*, Reno, NV, January 2006. AIAA Paper 2006-304.

[40] H. T. Huynh. A flux reconstruction approach to high order schemes including discontinuous galekin methods. In *17th. AIAA Computational Fluid Dynamics Conference*, Miami, Florida, 2007. AIAA-2007-4079.

[41] K. Van den Abeele, C. Lacor, and Z.J. Wang. On the connexion between the spectral volume and spectral difference method. *Journal of Computational Physics*, 227:877–885, 2007.

[42] K. Van den Abeele, C. Lacor, and Z.J. Wang. On the stability and accuracy of the spectral difference method. *Journal of Scientific Computing*, 2008.

[43] K.C. Hall and W.S. Clark. Linearized Euler predictions of unsteady aerodynamic loads in cascades. *AIAA journal*, 31:540–550, 1993.

[44] K. C. Hall, J. P. Thomas, and W. S. Clark. Computation of unsteady nonlinear flows in cascades using a harmonic balance technique. In *9th International Symposium on Unsteady Aerodynamics, Aeroacoustics and Aeroelasticity of Turbomachines*, Lyon, France, September 2000.

[45] M. McMullen, A. Jameson, and J. Alonso. Acceleration of convergence to a periodic steady state in turbomachinery flows. In *39th. Aerospace Sciences Meeting and Exhibit*, Reno, NV, January 2001. AIAA Paper 01-0152.

[46] M. McMullen, A. Jameson, and J. Alonso. Application of a non-linear frequency domain solver to the Euler and Navier-Stokes equations. In *40th. Aerospace Sciences Meeting and Exhibit*, Reno, NV, January 2002. AIAA Paper 02-0120.

[47] S. Nadarajah. Convergence studies of the time accurate and non-linear frequency domain methods for optimum shape design. *International Journal of Computational Fluid Dynamics*, 21:189–207, 2007.

[48] A.R. Gopinath and A. Jameson. Time spectral method for periodic unsteady computations over two- and three- dimensional bodies. In *43th. Aerospace Sciences Meeting and Exhibit*, Reno, NV, January 2005. AIAA Paper 2005-1220.

[49] A.R. Gopinath and A. Jameson. Application of the time spectral method to periodic unsteady vortex shedding. In *44th. Aerospace Sciences Meeting and Exhibit*, Reno, NV, January 2006. AIAA Paper 2006-0449.

[50] V.V. Rusanov. Calculation of interaction of non-steady shock waves with obstacles. *USSR Journal of Computational Mathematics and Mathematical Physics*, 1:267–279, 1961.

[51] P.L. Roe. Approximate Riemann solvers, parameter vectors and difference schemes. *Journal of Computational Physics*, 189:357–372, 1981.

[52] R. Swanson and E. Turkel. Multistage schemes with multigrid for Euler and Navier-Stokes equations - components and analysis. NASA Technical Paper 3631, August 1997.

[53] B. Van Leer, L. Wen-Tzong, P.L. Roe, and K.G. Powell. Design of optimally smoothing multi-stage schemes for the euler equations. In *9th AIAA Computational Fluid Dynamics Conference*, Orlando, Florida, 1989. AIAA Paper 89-1933.

[54] Y. Sun, Z.J. Wang, Y. Liu, and C.L. Chen. Efficient implicit LU-SGS algorithm for high-order spectral difference method on unstructured hexahedral grids. In *45th Aerospace Sciences Meeting and Exhibit*, Reno, NV, January 2007. AIAA Paper 2007-0313.

[55] M. McMullen. *The Application of a Non-Linear Frequency Domain Solver to the Euler and Navier-Stokes Equations.* PhD thesis, Departement of Aeronautics and Astronautics, Stanford University, Stanford, CA, March 2003.

[56] K. Fidkwoski. A high-order discontinuous galerkin multigird solver for aerodynamic applications. Master's thesis, Departement of Aeronautics and Astronautics, Massachusetts Institute of Technology, June 2004.

[57] V. Venkatakrishnan, S.R. Allmaras, D.S. Kamenetski, and F.T. Johnson. Higher order schemes for the compressible Navier-Stokes equations. In *16th AIAA Computational Fluid Dynamics Conference*, Orlando, Florida, June 2003. AIAA Paper No. 2003-3987.

[58] S.S. Davis. NACA 64A101 (NASA ames model) oscillatory pitching. In *AGARD report 702.* AGARD, January 1982.